

AD-A146 266

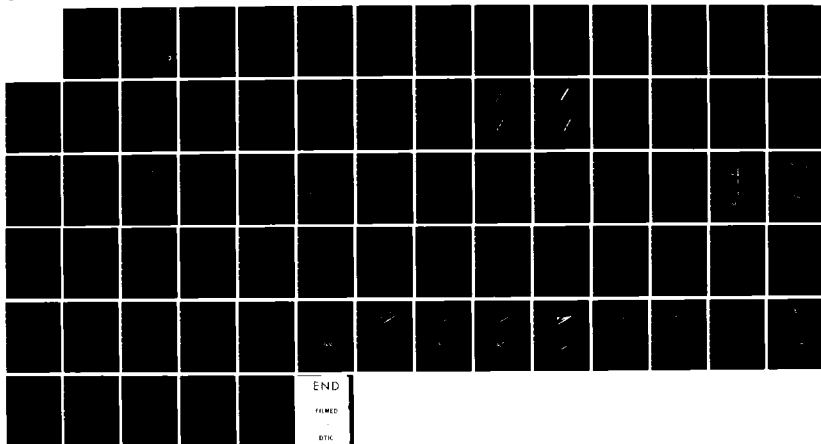
MOVING FINITE ELEMENTS IN 2-D(U) SCIENCE APPLICATIONS
INC PLEASANTON CALIF R J GELINAS 06 AUG 84 SAI-84/1299
AFOSR-TR-84-0832 F49620-81-C-0073

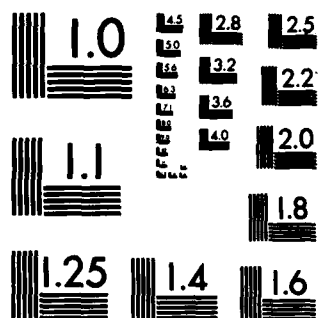
1/1

UNCLASSIFIED

F/G 12/1

NL





MICROCOPY RESOLUTION TEST CHART
NATIONAL BUREAU OF STANDARDS-1963-A

AD-A146 266

MOVING FINITE ELEMENTS IN 2-D

Final Report

AFOSR Contract: F49620-81-C-0073
Program Manager: Captain John P. Thomas

Submitted by

Robert J. Gelinas,
Principal Investigator

Science Applications, Inc.
1811 Santa Rita Road
Pleasanton, CA 94566

(415) 462-5300

August 6, 1984

DTIC
ELECTE
SEP 28 1984
S D E

DTIC FILE COPY

Approved for public release; distribution unlimited

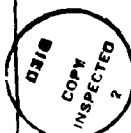
REPORT DOCUMENTATION PAGE

REPORT SECURITY CLASSIFICATION UNCLASSIFIED		1b. RESTRICTIVE MARKINGS	
SECURITY CLASSIFICATION AUTHORITY		3. DISTRIBUTION AVAILABILITY OF REPORT Approved for public release; distribution unlimited.	
DECLASSIFICATION/DOWNGRADING SCHEDULE		5. MONITORING ORGANIZATION REPORT NUMBER(S) AFOSR-TR-84	
PERFORMING ORGANIZATION REPORT NUMBER(S)		7a. NAME OF MONITORING ORGANIZATION Air Force Office of Scientific Research	
NAME OF PERFORMING ORGANIZATION Science Applications, Inc.	6b. OFFICE SYMBOL (If applicable)	7b. ADDRESS (City, State, and ZIP Code) Directorate of Mathematical & Information Sciences, AFOSR, Bolling AFB DC 20332	
ADDRESS (City, State, and ZIP Code) 1811 Santa Rita Road, Suite 104 Pleasanton CA 94566		9. PROCUREMENT INSTRUMENT IDENTIFICATION NUMBER F49620-81-C-0073	
NAME OF FUNDING/SPONSORING ORGANIZATION AFOSR	8b. OFFICE SYMBOL (If applicable) NM	10. SOURCE OF FUNDING NUMBERS	
ADDRESS (City, State, and ZIP Code) Bolling AFB DC 20332		PROGRAM ELEMENT NO. 61102F	PROJECT NO. 2304
		TASK NO. A3	WORK UNIT ACCESSION NO.
TITLE (Include Security Classification) MOVING FINITE ELEMENTS IN 2-D.			
PERSONAL AUTHOR(S) Robert J. Golinas			
TYPE OF REPORT Final	13b. TIME COVERED FROM 8/6/83 TO 7/6/84	14. DATE OF REPORT (Year, Month, Day) 6 AUG 84	15. PAGE COUNT 70
SUPPLEMENTARY NOTATION			
COSATI CODES		18. SUBJECT TERMS (Continue on reverse if necessary and identify by block number)	
FIELD	GROUP	SUB-GROUP	
ABSTRACT (Continue on reverse if necessary and identify by block number)		/node biasing effects.	
<p>The moving finite element (MFE) method is a new approach for numerically solving partial differential equation (PDE) systems; it is particularly well suited for resolving PDE solutions which may contain large, multiple gradients over highly disparate scales in both space and time. These types of PDE's abound in such basic technical disciplines as aerodynamics (with emphasis on shear layers, shocks and their possible interactions), combustion, plasma physics, material interface phenomena, continuum mechanics, and other transport processes.</p>			
(CONTINUED)			
21. DISTRIBUTION AVAILABILITY OF ABSTRACT <input checked="" type="checkbox"/> UNCLASSIFIED UNLIMITED <input type="checkbox"/> SAME AS RPT <input type="checkbox"/> DTIC USERS		21. ABSTRACT SECURITY CLASSIFICATION UNCLASSIFIED	
22. NAME OF RESPONSIBLE INDIVIDUAL CPT John P. Thomas, Jr.		22b. TELEPHONE (Include Area Code) 202 774 5026	22c. OFFICE SYMBOL NM

ITEM #19, ABSTRACT, CONTINUED:

In the MFE method, grid co-ordinates themselves are dependent variables which are calculated continuously at each time step in order to minimize PDE residuals. This feature has successfully suppressed numerical dissipation to very low levels and has resolved accurately in 1-D those physical transport processes which may occur over extremely small scales simultaneously with other physical processes which may span macroscopic scales. The objectives of the presently reported research effort were to extend the MFE method to 2-D and to investigate its basic properties and needs for solving important PDE's in 2-D. This, of course, is an on-going effort which is in only the early stages of discovery and development. This report describes the work tasks and results which have contributed to attainment of the objectives cited above.

Accession For	
NTIS GRA&I	<input checked="" type="checkbox"/>
DTIC TAB	<input type="checkbox"/>
Unannounced	<input type="checkbox"/>
Justification	
By	
Distribution/	
Availability Codes	
Dist	Avail and/or Special
A-1	



INTRODUCTION

AFOSR Technical Report 88-01
AFOSR Division

The moving finite element (MFE) method is a new approach for numerically solving partial differential equation (PDE) systems;^(1,2,3) it is particularly well suited for resolving PDE solutions which may contain large, multiple gradients over highly disparate scales in both space and time. These types of PDE's abound in such basic technical disciplines as aerodynamics (with emphasis on shear layers, shocks and their possible interactions), combustion, plasma physics, material interface phenomena, continuum mechanics, and other transport processes.

In the MFE method, grid co-ordinates themselves are dependent variables which are calculated continuously at each time step in order to minimize PDE residuals. This feature has successfully suppressed numerical dissipation to very low levels and has resolved accurately in 1-D those physical transport processes which may occur over extremely small scales simultaneously with other physical processes which may span macroscopic scales. The objectives of the presently reported research effort were to extend the MFE method to 2-D and to investigate its basic properties and needs for solving important PDE's in 2-D. This, of course, is an on-going effort which is in only the early stages of discovery and development. This report describes the work tasks and results which have contributed to attainment of the objectives cited above. The results of work performed to date can be summarized briefly as an introduction to the more detailed reporting which follows in subsequent sections.

It was established during the first year of this study that the MFE method does indeed extend logically and practically to 2-D. This fact has been substantiated in recent work by others as well.⁵ An initial experimental 2-D MFE code version was developed in the first year of our work under AFOSR support for the purpose of conducting continuing theoretical and applied mathematical research in diverse scientific contexts. Also in the first year of study, effective MFE node movement properties and significant node savings were demonstrated for simple -- but yet significant --

problems in 2-D. The MFE code structure was found to be amenable to vectorization and use on envisioned advanced computers. Work during the second year of study focussed on such essential issues and research needs as ODE integrators for numerical PDE solution methods, MFE regularization functions, grid node biasing effects, and linear solvers for large skewed matrices which do not contain diagonally dominant terms. Work in the third year has addressed the possible resolution of highly disparate PDE scales in order to analyze physical dissipation effects in shocks, distinct from artificial or purely numerical diffusion effects. This has involved development in the MFE method of physical, non-slip boundary conditions and of improved numerical conditioning of matrix solvers for the discretized equations of the MFE method. Detailed accounts of research during this three year project are presented in the report which follows.

I. Mathematical Background of the MFE Method

In order to present a coherent report of work to the broadest range of readers, we present here a brief mathematical sketch of the MFE method. Consider a general system of partial differential equations (PDE's), $\dot{U} = L(U)$ or

$$\begin{aligned}\dot{u}_1 &= L_1(U) \quad , \\ \dot{u}_N &= L_N(U) \quad .\end{aligned}\tag{1}$$

Using piecewise linear approximinants of $u_1 \dots u_N$,* which are of the form $u = mx + ny + p$, on a hexagonally connected triangular mesh (Figures 1-4), application of the chain rule to the differentiation of u_k gives:

$$\dot{u}_k = \sum_j \dot{a}_j \alpha_k^j + \dot{x}_j \beta_k^j + \dot{y}_j \gamma_k^j \quad , \text{ where} \tag{2}$$

$$\alpha_k^j = \alpha^j = \frac{\partial u_k}{\partial a_j} ; \beta_k^j = \frac{\partial u_k}{\partial x_j} ; \gamma_k^j = \frac{\partial u_k}{\partial y_j} \quad . \tag{3}$$

The key aspect of the MFE method lies in the rigorous retention of the nodal motion terms involving \dot{x} and \dot{y} . In most conventional PDE solution methods, the nodal motion terms are either set to zero (fixed nodes) or allowed to assume some arbitrary selected values (e.g., mean fluid velocities in Lagrangian codes).

Alternatively, the MFE method uses a very fundamental criterion for the evaluation of grid node motions (\dot{x} and \dot{y}) at every time step. That is, the basic MFE method is formulated by requiring that all of the time derivatives $\dot{a}_1, \dots, \dot{a}_N, \dot{x}_j, \dot{y}_j$ be found at each instant in such a way as to minimize the L^2 norm of the PDE residual, $||\dot{U} - L(U)||$. This has been found to minimize PDE solution errors and to dramatically reduce the number of grid

*The present mesh triangulation has been chosen for simplicity. Many other grid meshing schemes are, of course, possible; and many of the alternative schemes should be investigated in future work. It is interesting to note, however, that numerous MFE results confirm that PDE solution approximants of higher degree are not nearly so critical for attaining high levels of stability, accuracy and resolution in an optimal moving node solution method as they are in fixed node or less optimal adaptive PDE solution methods.

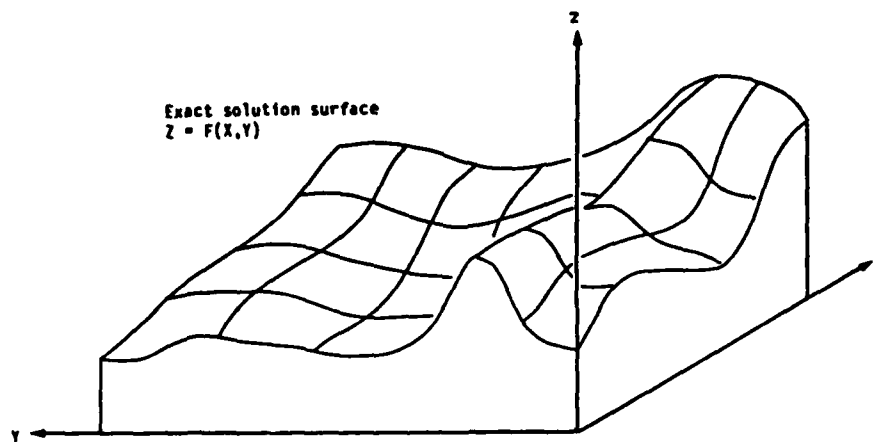


Figure 1. Exact solution surface, with lines of constant X and constant Y .

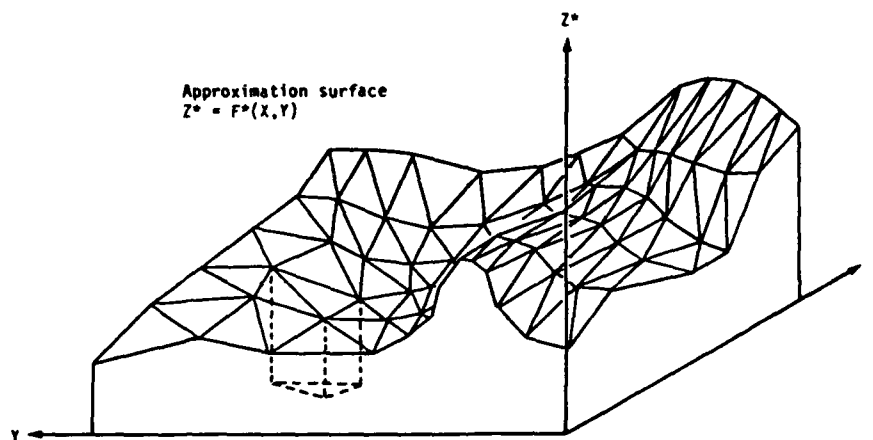


Figure 2. Approximate solution represented by piecewise linear functions making up triangular facets.

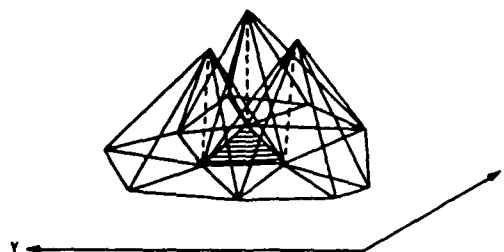


Figure 3. Basis functions defined on each hexagon provide three linearly independent basis functions on each triangle of the entire problem domain.

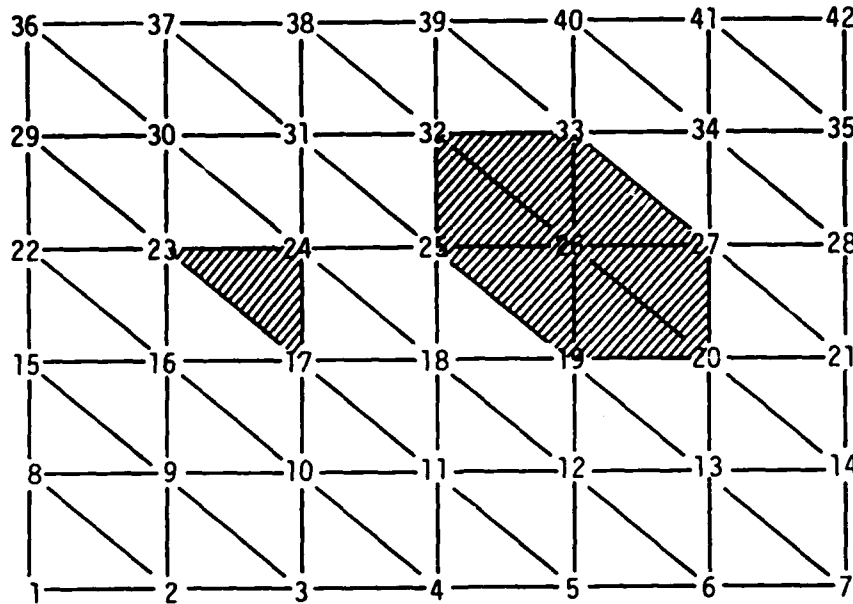


Figure 4. MFE Nodal Grid.

nodes. In order to handle the degeneracies which can sometimes occur in such a parametrization of PDE solutions, regularization techniques are applied. That is, the more general function,

$$\psi \equiv w_1^2 || \dot{u}_1 - L_1(U) ||^2 + \dots w_N^2 || \dot{u}_N - L_N(U) ||^2 + \sum_{\substack{\text{triangle} \\ \text{altitudes}}} (\epsilon_j \dot{h}_j - S_j)^2,$$

is minimized with respect to the parameter derivatives $\dot{a}_1, \dots, \dot{a}_N, \dot{x}_j, \dot{y}_j$. The present code applies the most elementary form of regularization functions in which the expressions for $\epsilon_j^2(d_j)$ and $\epsilon_j S_j = \epsilon_j(d_j) S_j(d_j)$ become extremely large and thus restrict node motions when any triangle altitude d_j approaches a user-specified minimum separation tolerance. Regularization techniques also serve to move nodes according to certain physical criteria in addition to providing numerically well-conditioned node movement properties. The variational equations for this minimization procedure are then represented by the large set of ODE's which follows:

$$\sum_j [(\alpha^j, \alpha^i) \dot{a}_{kj} + (\beta^j, \alpha^i) \dot{x}_j + (\gamma^j, \alpha^i) \dot{y}_j] =$$

(4a)

$$(L_k(U), \alpha^i) \text{ for } k = 1, \dots, N,$$

$$\sum_{k=1}^N w_k^2 \sum_j \left[(\alpha^j, \beta_k^i) \dot{a}_{k_j} + (\beta_k^j, \beta_k^i) \dot{x}_j + (\gamma_k^j, \beta_k^i) \dot{y}_j \right] = \quad (4b)$$

$$\sum_{k=1}^N w_k^2 (L_k(U), \beta_k^i) + (\text{regularization terms})$$

$$\sum_{k=1}^N w_k^2 \sum_j \left[(\alpha^j, \gamma_k^i) \dot{a}_{k_j} + (\beta_k^j, \gamma_k^i) \dot{x}_j + (\gamma_k^j, \gamma_k^i) \dot{y}_j \right] = \quad (4c)$$

$$\sum_{k=1}^N w_k^2 (L_k(U), \gamma_k^i) + (\text{regularization terms})$$

The sums on j in Equations (4) run over the seven neighboring nodes of i (including the i th node itself) in the hexagonal grid. Equations (4) thus provide the basic working equations of the MFE method in 2-D. This system of ODE's is of the form

$$R(y) \equiv C(y)\dot{y} - g(y) = 0, \quad (5)$$

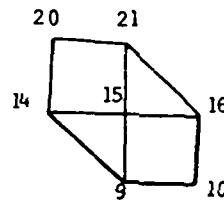
where $y(t) = (a_1, \dots, x_1, y_1; a_2, \dots, x_2, y_2; \dots)$ is the vector of unknown parameters, and the "mass matrix" $C(y)$ is symmetric and positive definite. This system of ODE's can be quite stiff, and stiff ODE solution methods are thus required in order to effectively obtain the numerical solutions of Equations (4) and (5). Research which attempts to eliminate this stiffness feature is in a very early stage of investigation, and preliminary results are not reported at this time.

The stiffly stable numerical integration methods which can be used to solve the system of ordinary differential equations (4) and (5) usually contain a series of backward Cauchy-Euler steps interspersed with interpolations and extrapolations, all amidst error-controlling tests and strategies. A backward Cauchy-Euler (BCE) step is obtained by replacing \dot{y} in Equation (5) by the backward difference $(y - \tilde{y})/\Delta t$, where \tilde{y} is the known parameter vector at the previous time, and y is the unknown parameter vector at the current time. Upon linearization, the BCE equation then reads as

$$R(y, \tilde{y}) \approx R(\tilde{y}) + R'(\tilde{y}) \cdot \delta y = 0 \quad (6)$$

The structure of the mass matrix $C(y)$ determines in large measure the degree of difficulty and computational cost of obtaining numerical solutions for δy in Equation (6) and thus for the y array in Equations (4) and (5). Both an implicit Runge-Kutta method (DIRK2) and the Gear method are used interchangeably in the present test MFE code in 2-D; both of these stiff ODE solvers incorporate the backward Cauchy-Euler steps described above.

The structure of the mass matrix $C(y)$ can be seen by considering the 15th node in a 6 x 6 grid mesh of the type shown in Figures 1-4. The coupling among nodes in Equation (4) is represented schematically by



and the block structure of the mass matrix is shown in Figure 5. For a PDE system with 2 "problem variables," the segment of the dependent variable array y associated with the 15th node is $(y)_{15} = (a_{15}, a_{25}, x_{15}, y_{15})^*$, and the 4 x 4 block $C_{15,16}$ is

$$C_{15,16} = \begin{bmatrix} (a_{16}, a_{15}) & 0 & (b_{16}, a_{15}) & (\gamma_{16}, a_{15}) \\ 0 & (a_{16}, a_{15}) & (b_{26}, a_{15}) & (\gamma_{26}, a_{15}) \\ (a_{16}, b_{15}) & (a_{16}, b_{25}) & \sum_{k=1}^2 (b_{k6}, b_{k15}) & \sum_{k=1}^2 (\gamma_{k6}, b_{k15}) \\ (a_{16}, \gamma_{15}) & (a_{16}, \gamma_{25}) & \sum_{k=1}^2 (b_{k6}, \gamma_{k15}) & \sum_{k=1}^2 (\gamma_{k6}, \gamma_{k15}) \end{bmatrix} \quad (7)$$

*The co-ordinate variable y_{15} of the 15th MFE node is not to be confused with the dependent variable of the MFE method which is also denoted by y .

Although direct L-U decomposition and solution of Equation (6) is relatively slow, it is reliable and was thus used in the initial code versions in the presently reported work. More efficient matrix solution methods remain under investigation.

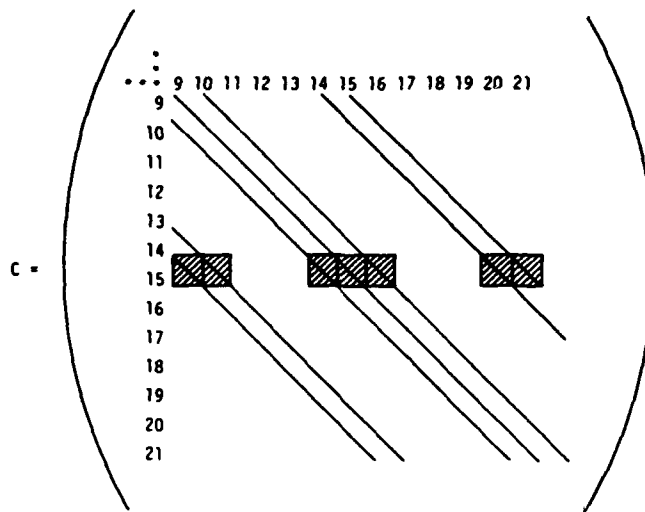


Figure 5. Block Structure of the Mass Matrix $C(y)$.

A large amount of the computational effort in the MFE method is devoted to repetitive evaluations of the inner product terms in Equations (4), which are then used iteratively in the numerical ODE integration procedures. Because invariant geometrical relationships can be exploited frequently in the evaluation of inner products, these geometrical relationships are generated and encoded once, and for all time, from the initialization data at the outset of code calculations. Figures 6-8 illustrate the grid mesh conventions which would be established and encoded by the present 2-D research code for 42 nodes on a 7 x 6 grid. The manner in which these relationships are used can be seen readily by considering a single conservation equation

$$u_t = -f_x - g_y + u_{xx} + u_{yy} \quad (8)$$

and the piecewise linear basis functions about the i th node of the form

$$\alpha_j = a_j x + b_j y + c_j \quad (9)$$

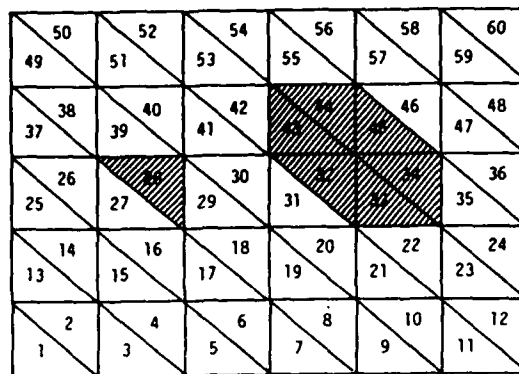


Figure 6. Triangles.

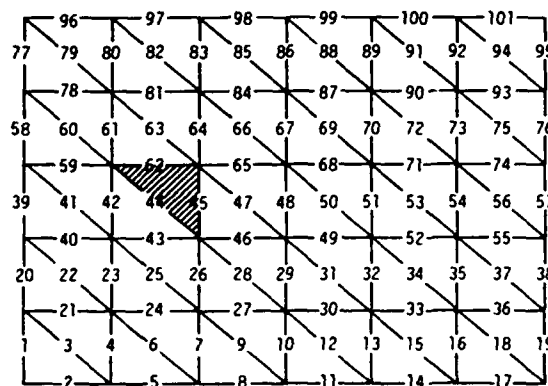


Figure 7. Edges.

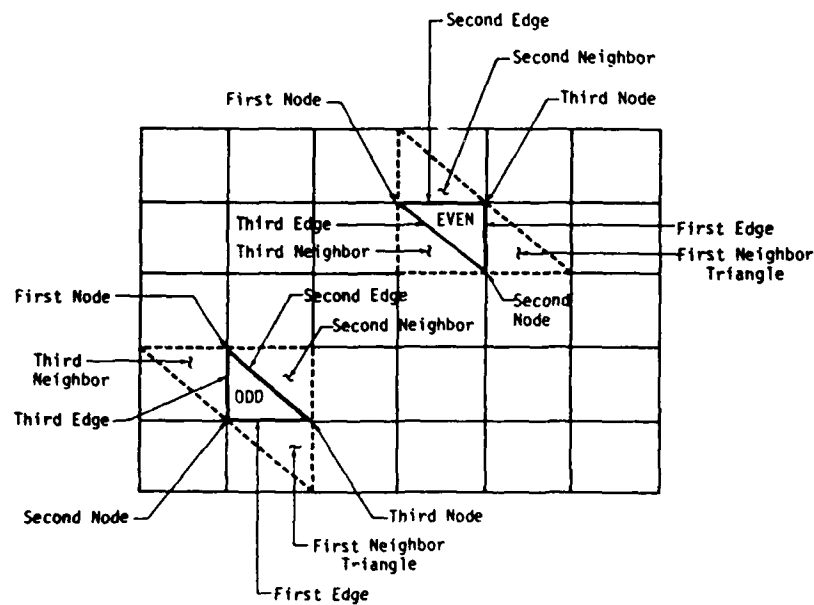


Figure 8. Triangle Conventions.

The inner products (α_i, α_i) which appear in the mass matrix of Equations (4) are evaluated as

$$(\alpha_i, \alpha_i) = \int_{6T} dx dy (a_i x + b_i y + c_i)^2, \quad (10)$$

where the i^{th} node is surrounded by six adjoining triangles T . The two-dimensional integration over a triangle T in Equation (10) can be performed either analytically or by the midpoint rule according to the formula

$$\int w(x, y) dx dy \approx (A/3) [w(P_1) + w(P_2) + w(P_3)], \quad (11)$$

where A is the area of triangle T , and P_1, P_2 , and P_3 are the midpoints of the sides. This simple midpoint formula of integration is exact whenever the integrand, $w(x, y)$ is a quadratic function in x and y . The present research code uses the above midpoint rule and contains options for the use of a composite midpoint and some analytic integration methods, as well. Using the relationships between basis functions $\beta_i = u_x \alpha_i$ and $\gamma_i = u_y \alpha_i$, and noting that u_x and u_y are constants, the inner products (α_i, β_i) , (β_i, β_i) , (β_i, γ_i) and (γ_i, γ_i) can also be evaluated by the midpoint rules. For a general operator $L(u) = f$, it can be shown that

$$(-f_x, \alpha_i) = \sum (\alpha_x)_i \int dx dy f, \quad \text{and} \quad (12)$$

$$(-f_x, \beta_i) = \sum u_x \left\{ -(\alpha_x)_i \int dx dy f + \sum_{\substack{2 \text{ inner} \\ \text{edges of } T}} n_1 \int f \tau(s) ds \right\}. \quad (13)$$

The integration on ds is performed with respect to arc length s along a triangle edge and $\alpha_i = \tau(s)$ is the linear function of s which rises from a value 0. at an outer node to a value 1.0 at the i^{th} central node. Edge integrals can be evaluated analytically or by numerical quadrature. Simpson's rule and a composite Simpson's rule are available for use in the present research code. The derivatives α_x, u_x , and the x component of the unit outward normal n_1 are readily determined at all times by invariant formulae from the known amplitudes and nodal co-ordinates at triangle vertices.

Inner products of Laplacian operators are more complicated to evaluate, requiring, in addition to the quantities above, the unit tangent vectors and their x and y components.⁽⁶⁾ The formulae for these quantities are also encoded at the outset of computations for repeated use in later code calculations.

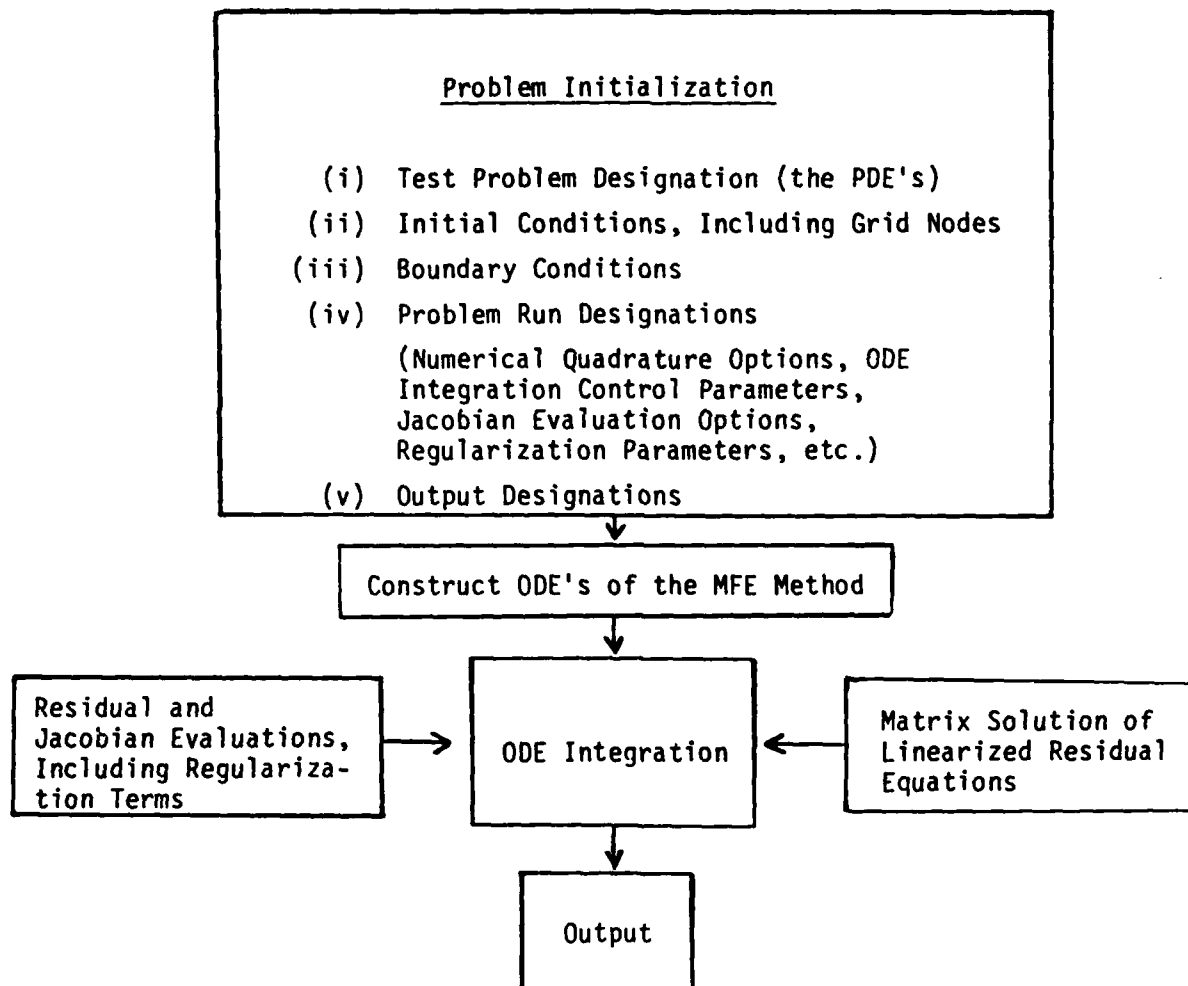


Figure 9. Schematic Representation of Major Functions Performed in the Present MFE Codes in Both 1-D and 2-D.

The overall 2-D code structure is conceptually simple, as indicated in Figure 9. The detailed code structure contains an assembly of approximately forty subroutines which perform modularly the numerous subtasks which are required in order to execute the major code functions indicated in Figure 9. This structure is intended to facilitate mathematical research on alternative (actually, interchangeable) ODE solution methods, matrix solution methods, node control strategies, boundary conditions, and such other tasks as grid mesh generation and issues of numerical analysis which must be investigated in new PDE solution methods. This code structure of the MFE method also appears to be highly compatible with vector and parallel processing computers.

Because the mass matrix $C(y)$ in Equation (5) can become singular (when- ever all components u have a flat portion in their graph at some node (x_i, y_i)), regularization terms are included in the minimization problem for the x and y equations. The minimization problem for \dot{x} and \dot{y} reads $\frac{\partial \psi}{\partial \dot{x}_k} = 0$ and $\frac{\partial \psi}{\partial \dot{y}_k} = 0$, where

$$\psi \equiv \sum_i w_i^2 || \dot{u}_i - L_i(u) ||^2 + \sum_{\substack{\text{triangle} \\ \text{altitudes}}} (\epsilon_j(\dot{d}_j) d_j - S_j(d_j))^2. \quad (14)$$

This minimization yields regularization terms of the form:

in the \dot{x} equation

$$\epsilon_j \left\{ \epsilon_j \dot{d}_j - S_j(d) \right\} \cdot \frac{\partial \dot{d}_j}{\partial \dot{x}_k} \quad (15a)$$

in the \dot{y} equation

$$\epsilon \left\{ \epsilon_j \dot{d}_j - S_j(d_j) \right\} \cdot \frac{\partial \dot{d}_j}{\partial \dot{y}_k} \quad (15b)$$

It follows that the terms $\dot{d}_j = \frac{\partial d}{\partial x_k} \dot{x}_k + \frac{\partial d}{\partial y_k} \dot{y}_k$ and the terms $\frac{\partial \dot{d}_j}{\partial \dot{x}_k}$ and $\frac{\partial \dot{d}_j}{\partial \dot{y}_k}$

in Equations (15) are dependent primarily upon grid geometry; and their invariant formulae are thus generated at the outset and encoded for repeated calculations later in the code in a manner similar to many portions of the residual evaluations which were discussed above.

The functions ϵ^2 and ϵS which appear in Equations (15) are treated in exactly the same manner as an advanced penalty function formulation which has been tested previously in 1-D investigations^(1,2) of effective regularization methods; that is,

$$\epsilon^2 = \frac{C_1}{(d - \text{SEPMIN})} \quad (16)$$

$$\epsilon S = \frac{C_2}{(d - \text{SEPMIN})^2} \quad (17)$$

where SEPMIN is a minimum triangle altitude. A detailed node controlling policy has been developed for the selection of values for the constants C_1 and C_2 in terms of local truncation errors and of the inner products (β, β) and (γ, γ) which appear in the x and y equations. A discussion of this policy in specific 1-D problem applications appears in References 1 and 2. A detailed discussion of this policy for 2-D applications is deferred until several additional generalizations are discussed. These generalizations will also have the effect of preventing automatically the inversions (tangling) of triangles. Such inversions are presently detected and prevented by testing the aspect ratios and the signs of triangle determinant quantities. Integration time steps are reduced when aspect ratios exceed a designated value or when there is a change of sign in the determinant quantities.

Numerous sample problems have been used for testing of the MFE method in 2-D. These problems have been designed to test such numerical aspects of the MFE method as:

- (1) Inner product evaluations (analytic and numerical quadrature)
- (2) ODE integration for the MFE equations
- (3) Matrix solution methods

- (4) Regularization schemes for control of node motions
- (5) Jacobian evaluations
- (6) Boundary conditions (zero-Neumann and Dirichlet).

The PDE's in these test problems are in the form of general conservation equations,

$$u_t = -f_x - g_y + v(u_{xx} + u_{yy}) , \quad (18)$$

where the flux functions f and g can have nearly arbitrary functional forms.

In addition to the simple examples of the heat equation and of square wave propagation which were presented in Reference 3, two somewhat more complex test examples have also been studied.

Oblique Propagation of a Scalar Wave

This example considers the propagation by pure advection of a scalar wave diagonally across the initial grid mesh, according to the equation $u_t + u_x + u_y = 0$. The initial conditions for this example are shown schematically in Figure 10 and are expressed as:

$$\begin{array}{ll} u(x,y,0) = 1.0 & 0.1 \leq x \leq 0.2; \quad 0.1 \leq y \leq 0.2 \\ u(x,y,0) = 0. & x \leq 0.05; \quad x \geq 0.25 \text{ and all } y \\ u(x,y,0) = \text{linear} & \text{otherwise} . \end{array}$$

Dirichlet conditions, $u(x,y,t) = 0.$, are applied at all boundaries. The co-ordinates x and y obey the following Dirichlet conditions: $x = 0.$ along the y axis; $x = 1.0$ along the boundary $x = 1.0$, all y , $y = 0.$ along the x axis; and $y = 1.0$ along the boundary $y = 1.0$, all x . The co-ordinate variables obey zero-Neumann conditions on y along the y axis and along the boundary at $x = 1.0$ for all y and on x along the x axis and along the boundary at $y = 1.0$ for all x . (That is, the y co-ordinate is free to slide along the vertical boundaries, and the x co-ordinate is free to slide along the horizontal boundaries.)

Using a 6x6 grid of moving nodes, this problem is run from $t = 0$. to $t = 0.8$, which spans the interval of free propagation. The accuracy of the wave profile is maintained to within 1 part in 10^3 , consistent with the local truncation error constraint in the ODE solver. The velocity of propagation is accurate to 4 significant figures. The mesh is observed to move flexibly in order to maintain these accuracies throughout the problem evolution. As this wave approaches the upper right-hand corner of the domain, aspect ratios of some of the grid mesh triangles approach values on the order of approximately 10^2 , with no adverse effects. The triangle aspect ratios can be made to assume values which are an order magnitude larger by imposing Dirichlet conditions on the x and y coordinates at the boundaries. It was also found that the MFE method can solve this problem with equal facility and efficiency for much larger, finite gradients of the scalar wave front.

This problem can readily be modified so that the scalar wave trajectory follows a circular path according to the pure advection equation,

$$u_t = \cos(t) \cdot u_x + \sin(t) \cdot u_y, \quad -a < x < a, -a < y < a, \quad (19)$$

where the dimensions a are sufficiently large to contain the circular trajectory. In this MFE solution, the scalar wave follows its circular trajectory accurately and returns precisely to its initial position, consistent with the local truncation error constraint in the ODE solver, after a complete revolution ($t = 2\pi$), using 20 time step cycles. The grid mesh again expands and contracts smoothly and flexibly in maintaining the desired solution accuracy at all times.

Burger-Like Equations.

A 2-D analog of Burger's 1-D model equation is given by the equations

$$\frac{\partial u}{\partial t} = -\frac{\partial(u^2)}{\partial x} - \frac{\partial}{\partial y}(uv) + v\nabla^2 u \quad (20)$$

$$\frac{\partial v}{\partial t} = -\frac{\partial}{\partial x}(uv) - \frac{\partial}{\partial y}(v^2) + v\nabla^2 v, \quad (21)$$

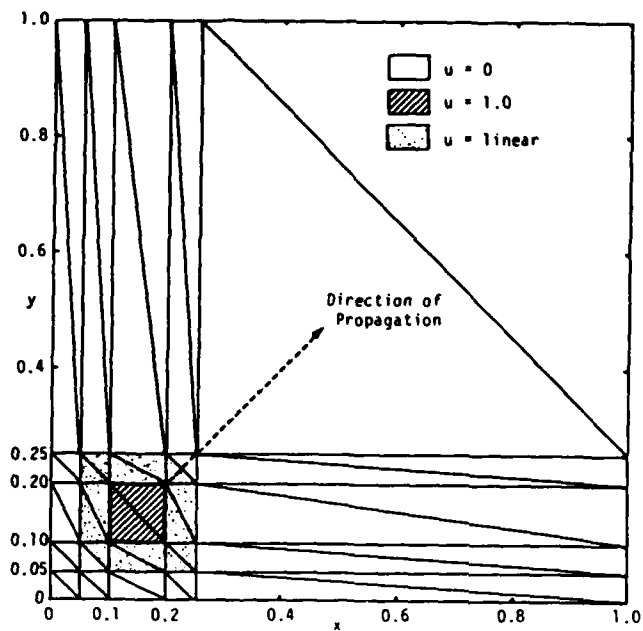


Figure 10. Initial Conditions for Oblique Propagation of Scalar Wave.

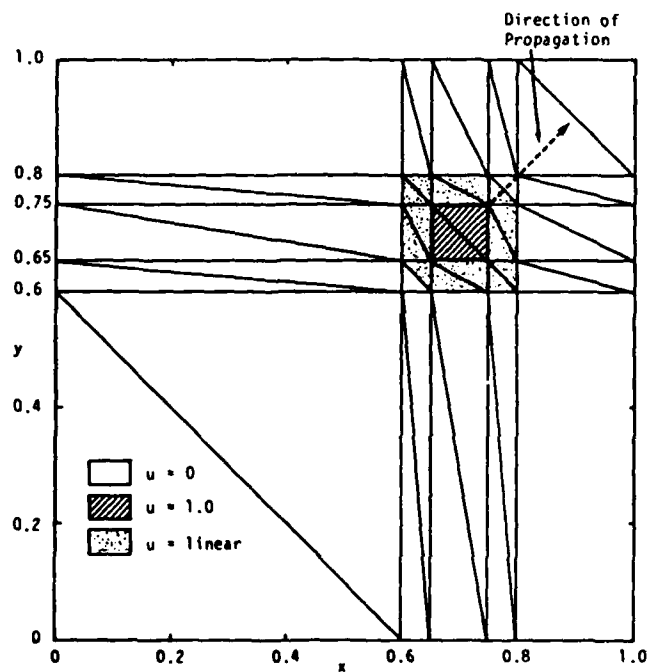


Figure 11. Transient Propagation of a Scalar Wave.

where u and v can be viewed as x and y components of a fluid velocity, respectively. In order to maintain a close analogy to the 1-D Burger's model results which were discussed in Reference 2, initial and boundary conditions for this system of PDE's are first selected so as to lead to the propagation of a uniform, step-like wave in a direction parallel to the x -axis; that is,

$$\begin{array}{ll} u(x,y,0) = 0. & 0. \leq x \leq 1.0; \quad 0. \leq y \leq 1.0 \\ v(x,y,0) = 1.0 & 0 \leq y \leq 0.100; \quad 0 \leq x \leq 1.0 \\ v(x,y,0) = 0. & 0.101 \leq y \leq 1.0; \quad 0 \leq x \leq 1.0 \\ v(x,y,0) = \text{linear} & \text{otherwise} \end{array}$$

This problem is solved from $t = 0$ to $t = 0.5$ on a 4×19 grid with $\nu = 10^{-2}$.^{*} The dependent variable v obeys zero-Neumann conditions along the y axis and along the (vertical) boundary at $x = 1.0$; and v obeys the Dirichlet conditions, $v = 1.0$ along the x axis and $v = 0.$ along the (horizontal) boundary at $y = 1.0$. All interior nodal co-ordinates obey the same type of sliding boundary conditions as were used in the scalar wave example discussed above. Figures 12-15 present the MFE solutions of this evolving wave front. The extensive migration of the MFE nodes from their initial positions to those positions which resolve the waveform at $t=0.2$ is clearly evident in Figures 12 and 13. The speed of propagation and the shock-like wavefront solutions are resolved to accuracies of three significant figures, or better, consistent with the local truncation error constraint of the ODE solver. The magnitudes of the wavefront gradients are approximately 100 in this example, and MFE solutions of this problem can be obtained with similar facility and efficiency for much larger gradients (corresponding to smaller values of ν in Equations (20) and (21)). Consistent with earlier results in Reference 7 for simple square wave propagation by pure advection, it is found also in this Burger-like example that wide latitude can be exercised in the selection of node controlling parameters in the functions ϵ^2 and ϵS of Equations (16)

^{*}This problem can be solved with equal effectiveness on an MFE grid of 4×10 nodes. The 4×19 grid simply represents the initial attempt on this problem. The figures 12-15 below have rotated the co-ordinate axes in the x - y plane by 90° from the conventional orientation (\hat{x} horizontal and \hat{y} vertical) in order to improve the viewing angle for the plotted results in 3-D. The terms "horizontal" and "vertical" refer strictly to the conventional orientation of the x - y plane throughout this discussion.

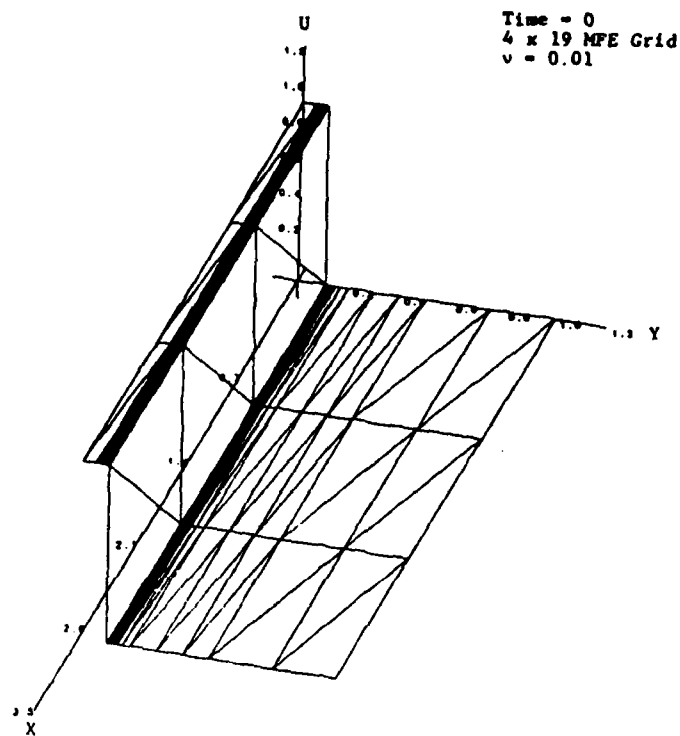


Figure 12. MFE Solution of Burger-like Equation in 2-D.

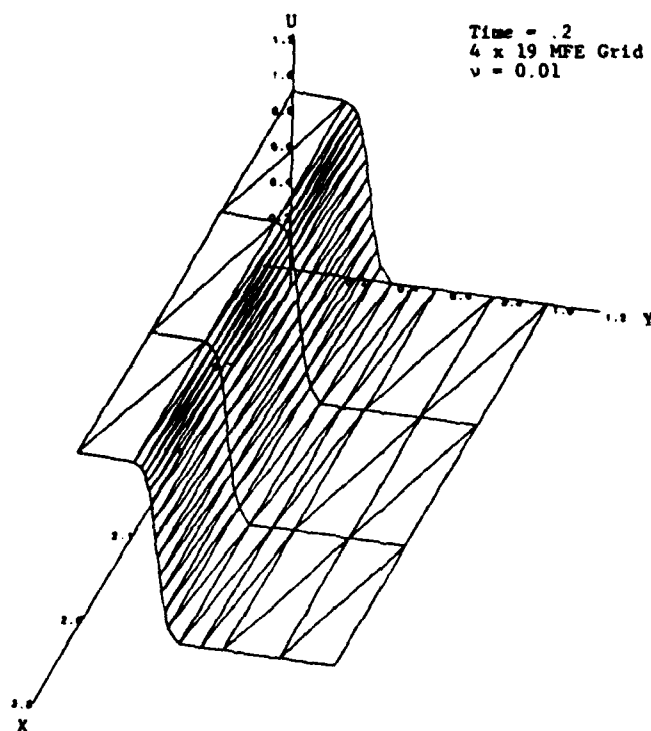


Figure 13. MFE Solution of Burger-like Equation in 2-D.

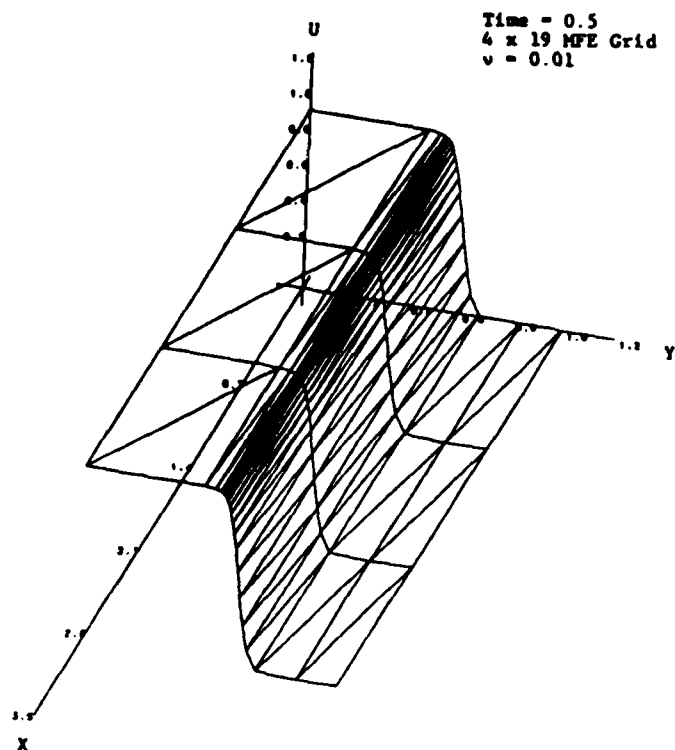


Figure 14. MFE Solution of Burger-like Equation in 2-D.

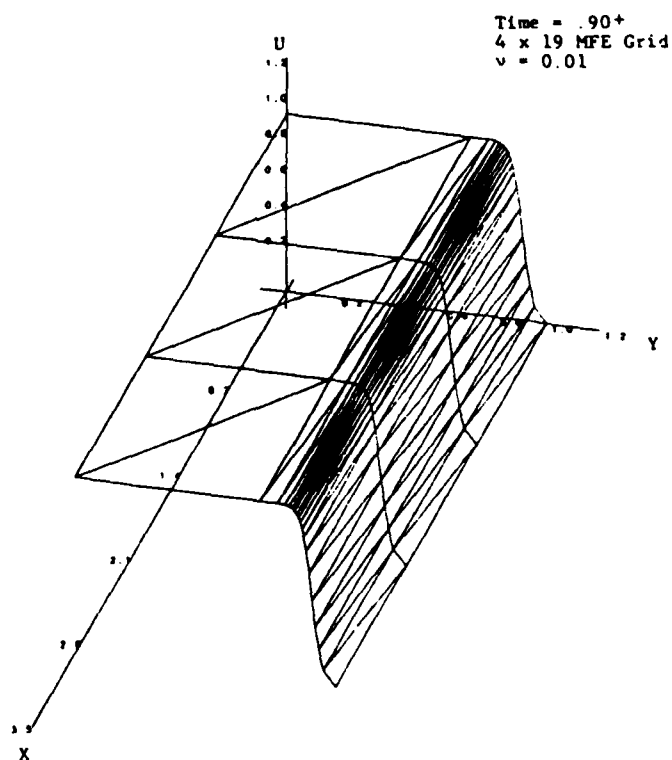


Figure 15. MFE Solution of Burger-like Equation in 2-D.

and (17). When relatively weak internodal forces are used, no nodal deviation (or bias) in the x direction is observed. (There are no transverse forces in the PDE's, per se.) As the internodal forces are increased to sufficiently large values, the nodes can be forced by the regularization terms to migrate toward the x -axis for the nodal triangulation shown in Figure 12--meanwhile maintaining the accuracies mentioned above. The direction of such forced nodal migration can be reversed by using the opposite type of grid triangulation, and this node migration can also be altered by the use of different penalty functions. Node control is thus very flexible and desired accuracies are readily maintained. When PDE's contain non-trivial x -dependencies in their operators, the PDE's themselves resume their dominant role in governing the positioning of the nodes, as will be seen in a skewed waveform example below. Figure 15 shows the formation of the boundary layer at the right-hand boundary, as this MFE solution approaches the correct asymptotic solution.

An example of a skewed, propagating wavefront (shock) can be formulated in terms of the Burger-like equations,

$$u_t = 0 \quad (22)$$

$$v_t = -1/2 (v^2)_y + v \nabla^2 v, \quad (23)$$

on the unit square. An 8×8 grid of MFE nodes is used, and the initial conditions for u and v on uniformly spaced grid nodes are:

$$\begin{aligned} u(x,y,0) &= 0 \quad \text{all } x,y \\ v(x,y,0) &= 1+7\tau, 1+6\tau, 1+5\tau, \dots, 1 \quad \text{at nodes } 1, 2, 3, \dots, 8 \\ &\quad \text{along 1st row (x-axis)} \\ v(x,y,0) &= -1, -(1+\tau), -(1+2\tau), \dots, -(1+7\tau) \quad \text{at nodes } 57, 58, \\ &\quad 59, \dots, 64 \quad \text{along top row.} \end{aligned}$$

The initial values of $v(x,y,0)$ along a given vertical line are obtained by linear interpolation at interior nodes. The parameter τ is assigned a

constant value of 0.01, and the value of v in Equations (22)-(23) is assigned a value of 0.01 in the present run. As shown in Figure 16, these initial conditions on v simply map a plane in which v has the values +1.07 at the coordinates (0,0); +1.0 at (1,0); -1.0 at (0,1); and -1.07 at (1,1). Dirichlet boundary conditions are maintained on $v(x,y,t)$ and on x and y along the horizontal boundaries; zero-Neumann boundary conditions are applied to $v(x,y,t)$ and to y on the vertical boundaries; and Dirichlet boundary conditions are maintained on x along the vertical boundaries. This skewing of the initially counter-directed velocity components along the top and bottom boundaries leads to the evolution of non-uniform wavefront solutions which are seen in the results below. In the early stages of solution, prior to $t = 0.5$, a projection of the MFE solution on the x - y plane shows two counter-directed, quasi-horizontal wave impulses which propagate from top to bottom and from bottom to top at speeds of approximately 0.5. At $t \approx 0.5$, a shock is formed when the propagating impulses encounter each other near the horizontal centerline of the x - y domain. Subsequently, a skewed, shock-like waveform is generated and propagates in the serpentine manner shown in Figures 16-19. The relatively large aspect ratios seen in Figure 19 for the MFE mesh at $t = 20$. were created deliberately by the use of Dirichlet boundary conditions on the x co-ordinates along the x axis and along the parallel boundary line at $y = 1$. The MFE node migration was fluid throughout and exhibited no grid-biasing effects. This problem was run from $t = 0$. to $t = 20$. in approximately 125 time-step cycles. The gradients of the fully developed shock are on the order of 100, consistent with the present value of $v = 0.01$. As above, MFE solutions of this problem on an 8×8 grid can be obtained for much larger gradients (smaller values of v) with essentially the same levels of robustness and efficiency as are seen in the present example.

From these early 2-D results it was apparent that the hexagonally connected triangular mesh and perhaps several other possible triangulation schemes are quite compatible with the MFE method. The additional degrees of geometrical freedom which are available for error minimizing node motions in 2-D have been found to have a beneficial effect on the numerical integration efficacy of the MFE method in 2-D, vis à vis the more highly constrained nodal motions in 1-D MFE solutions.^(7,8) The nodal movement properties observed in these initial 2-D results thus suggest some likely implications

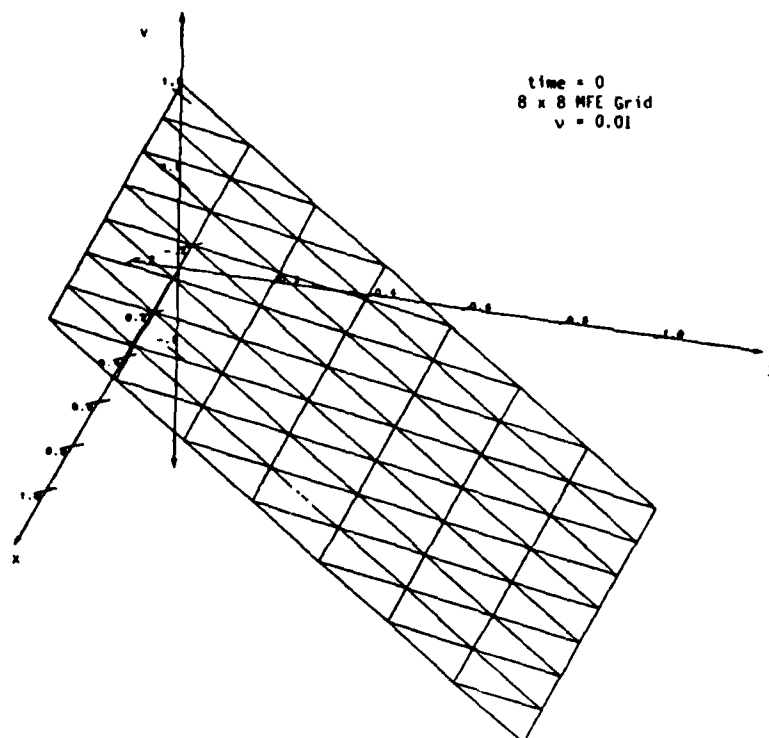


Figure 16. MFE Solution of Burger-like Equations for a Skewed Waveform in 2-D.

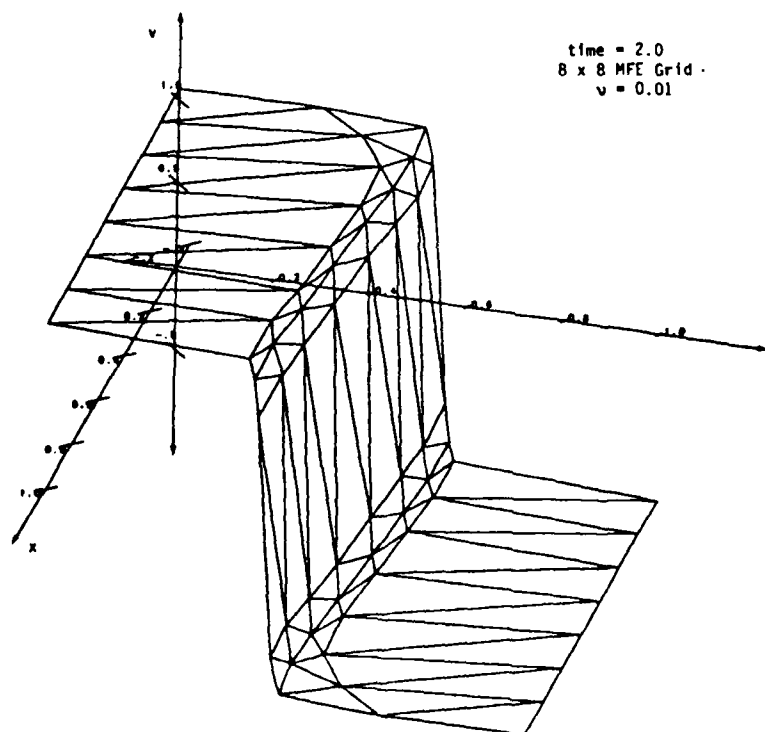


Figure 17. MFE Solution of Burger-like Equations for a Skewed Waveform in 2-D.

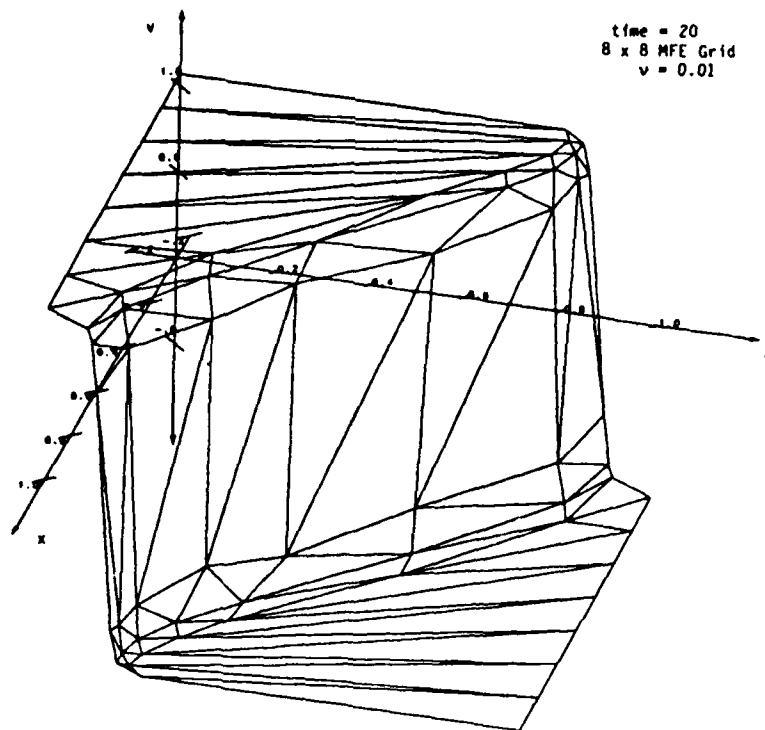


Figure 18. MFE Solution of Burger-like Equations for a Skewed Waveform in 2-D.

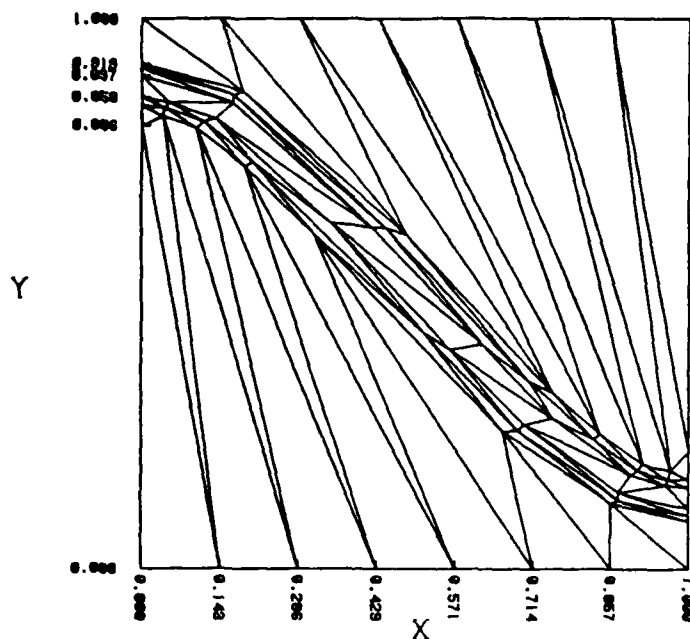


Figure 19. Projection on the x-y Plane of the MFE Solution of Burger-like Equations for a Skewed Waveform in 2-D. time = 20.; 8 x 8 MFE Grid; v = 0.01.

on the eventual role of mesh generation needs and data structure issues in the MFE method. So long as the MFE method exhibits this robustness in its continuous node movement properties, the use of grid mesh generation routines would be reduced primarily to problem initializations.

In order to study the MFE nodal migration properties under more demanding circumstances, the initial conditions for the Burger's model above can be extended so as to create a more highly skewed waveform in two directions. The PDE's for this skewed Burger's model problem are given by:

$$u_t = -uu_x - vu_y + v(u_{xx} + u_{yy}) \quad (24)$$

$$v_t = -uv_x - vv_y + v(v_{xx} + v_{yy}) \quad (25)$$

where u is the x -component of velocity and v is the y -component, and v is an effective diffusion coefficient. Shocks are generated with gradient magnitudes on the order of $1/v$. Initial conditions which produce a doubly skewed wavefront profile are shown schematically in Figures 20 and 21. (The counterposed initial velocity fields are designed to create an evolving shock profile which is skewed in both the x and y components of velocity.) Boundary conditions are given by:

$$\begin{array}{ll} u(0,y) = u(1,y) = 0 & 0. \leq y \leq 1. \\ v_x(0,y) = v_x(1,y) = 0. & 0. \leq y \leq 1. \\ u(x,1) = 0.2 \sin \pi x & 0. \leq x \leq 1. \\ u(x,0) = -.2 \sin \pi x & 0. \leq x \leq 1. \\ v(x,1) = -1. + 0.2 \cos \pi x & 0. \leq x \leq 1. \\ v(x,0) = 1. + 0.2 \cos \pi x & 0. \leq x \leq 1. \end{array}$$

The MFE nodes are fixed by zero Dirichlet conditions along the top and bottom horizontal edges of the domain. The nodes are free to move vertically by symmetric boundary conditions along the left and right edges of the domain.

This problem can be solved readily by perhaps many PDE solution methods whenever v assumes sufficiently large values. For example, a value of $v = 0.02$ produces shock gradients on the order of 10^2 .

The MFE method requires only an 8×8 grid to give reasonably accurate solutions to this problem, and Figures 22 and 23 show very accurate MFE solutions on a 12×12 grid. Here Figure 22 presents an isometric view of the evolving profile of the y component of velocity at $t = 3.0$, well after the shock has formed and after the wavefront has undergone significant shearing. The x -component of velocity is sufficiently sheared that a hidden line plot, which is not yet available, is required for easy interpretation by the naked eye. The MFE grid nodes have migrated extensively from their initial positions as can be seen in Figure 23 which represents the grid mesh projected onto the x - y plane at $t = 3.0$. Figures 24 and 25 present contour plots for selected constant values of u and v , respectively, at $t = 3.0$. It is evident from the magnitudes of shock gradients and from the regions of significant curvature which span nearly the entire domain that an alternative PDE method with a fixed grid may require on the order of 10^4 , or more, grid nodes in order to achieve comparable degrees of accuracy in this problem.

This same basic problem can now be made to correspond to a much more demanding physical problem by letting $\nu = 0.002$. Figure 26 shows an isometric view of the MFE solution on a 16×16 grid for this case. Shock gradients are now generated with magnitudes of several times 10^3 . Before discussing these MFE results in detail, some general observations should be discussed: It is likely that most existing PDE method using either a fixed grid or a less than optimal adaptive grid would require on the order of 10^5 - 10^6 grid nodes to solve this problem with comparable accuracy. (We note as an aside that numerous inviscid solvers which are under development do not apply at all to this type of advection-diffusion problem because the Laplacian is an essential mathematical operator whose effects must be rigorously resolved in advection-diffusion PDE's. Because inviscid solvers do not generally solve PDE's which contain Laplacians, they generate shocks with gradient shapes and magnitudes that are governed exclusively by the selected gridding and/or by the purely numerical dissipative processes in the inviscid method, per se. Consequently, inviscid solvers would have no chance of resolving correctly any of those physical dissipation effects which are usually expressed by Laplacian operators and are present with fundamental physical significance in transport theory, hydrodynamics, plasma physics, continuum mechanics, and many other disciplines in the physical sciences. This critical discussion

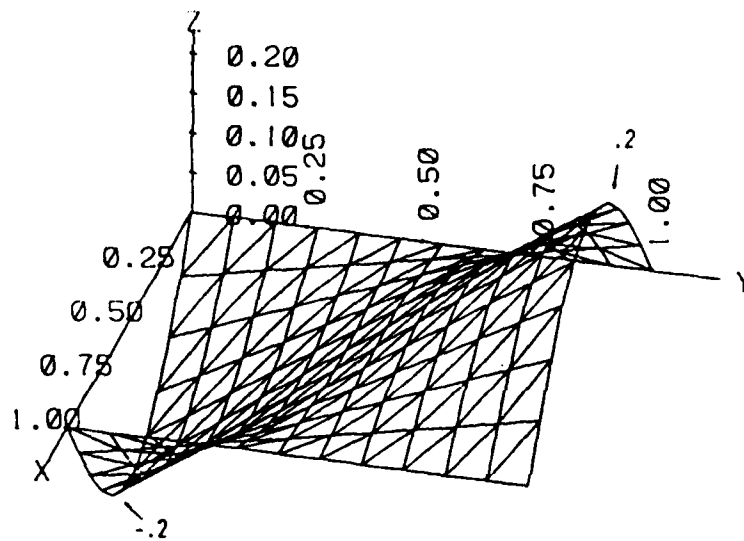


Figure 20. Plot of initial values of u in the 2-D Burger-like example on a 12×12 grid mesh.

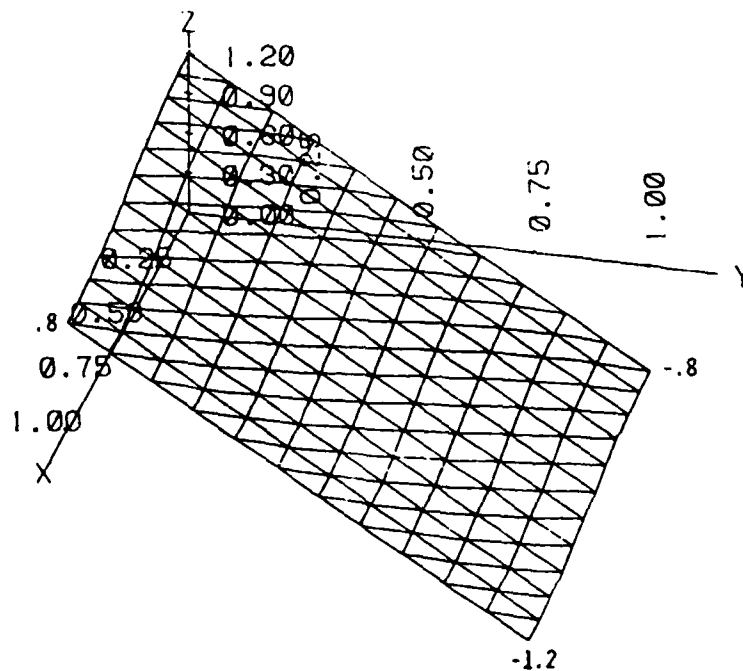


Figure 21. Plot of initial values of v in the 2-D Burger-like example on a 12×12 grid mesh.

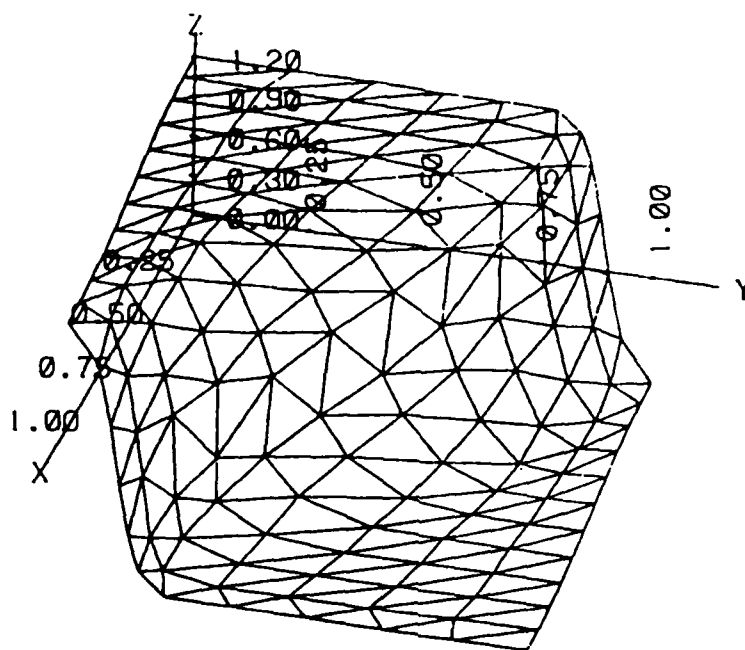


Figure 22. Isometric view of v at $t = 3.0$ in the 2-D Burger-like example on a 12×12 MFE grid.

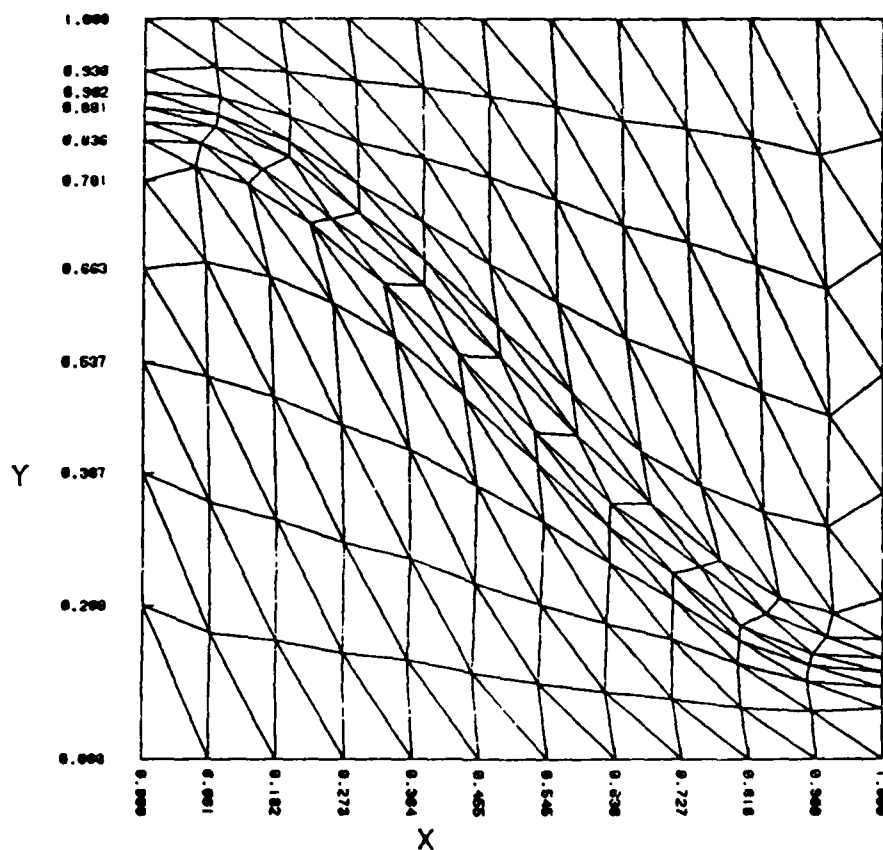


Figure 23. MFE grid projections on the X-Y plane at $t = 3.0$ in the 2-D Burger-like example on a 12×12 grid.

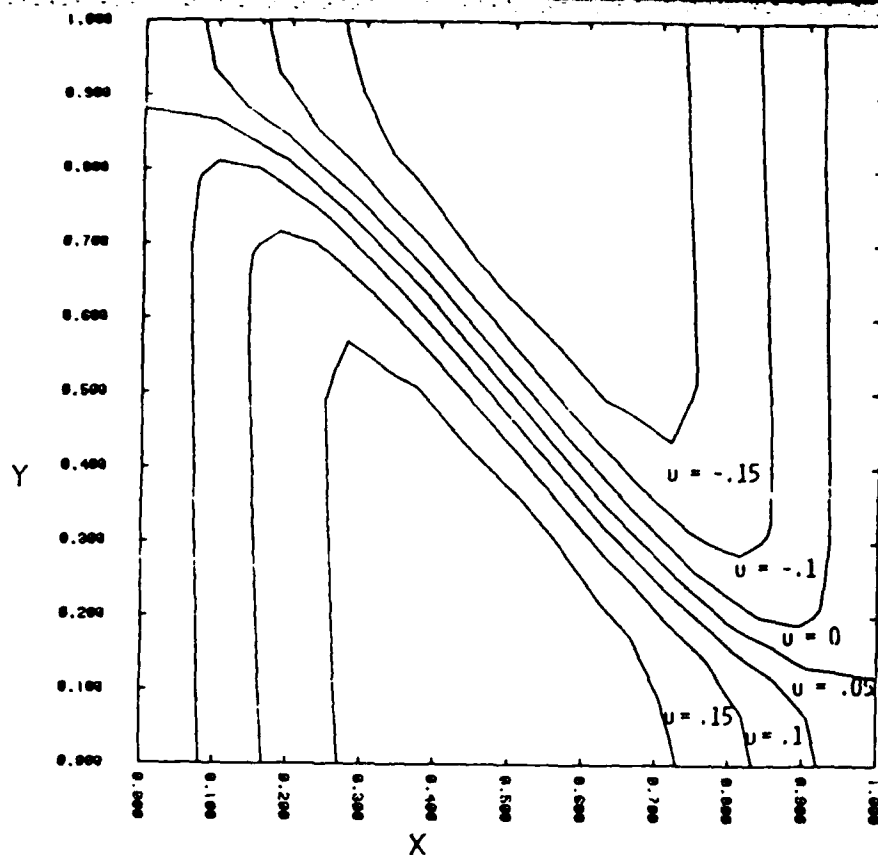


Figure 24. Contour plots of selected values of u at $t = 3.0$ in the 2-D Burger-like example on a 12×12 grid.

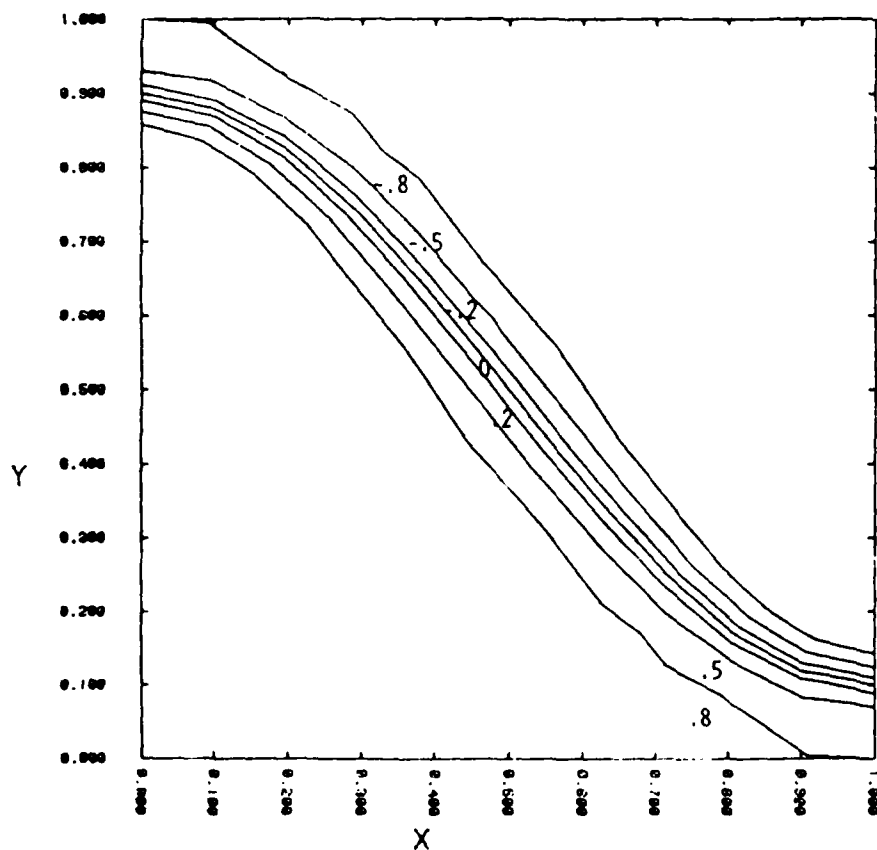


Figure 25. Contour plots of selected values of v at $t = 3.0$ in the 2-D Burger-like example on a 12×12 grid.

is not intended to denigrate the extensive research efforts on inviscid PDE solvers and/or fixed node PDE methods; but it does suggest that efforts to accommodate Laplacian operators in otherwise inviscid solution methods and efforts to investigate more optimal adaptive grid methods for use in many existing PDE methods which are applied to advection-diffusion problems should now assume greatly increased significance.)

It was apparent at this stage of research that our MFE results in 2-D were continuing a trend which appeared in previous 1-D results. There, MFE solutions of both the Navier-Stokes and physically dissipative continuum mechanics equations in 1-D exhibited perhaps unprecedented simultaneous

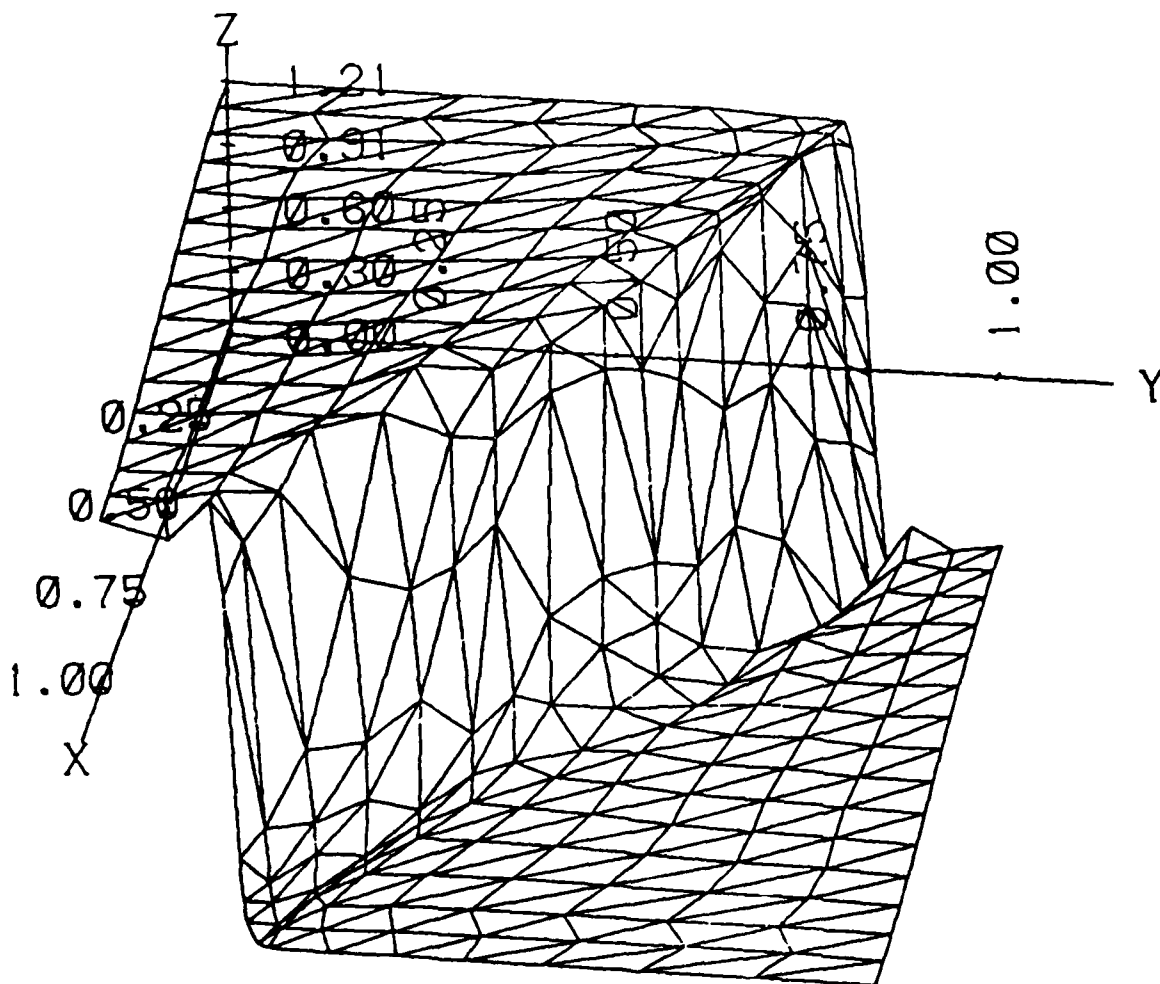


Figure 26. Isometric view of Burger's test example at $t = 1.8$ with $\nu = 0.002$ on a 16×16 MFE mesh. Shock gradients have magnitudes of approximately 10^3 in this solution for u .

resolution of extremely disparate microscale and macroscale physical processes.^(7,8) While 2-D MFE results which emerged during this period exhibit similar promising features, numerous mathematical problems still require resolution in order to attain fully the desired levels of success in truly large-scale physical problems in 2-D. Clues to these problems can be seen in Figure 26.* For example, the irregularity of the grid triangles in the face of the shock could eventually prove to be troublesome. Similarly, the small oscillation at the base of the shock in this run is unsatisfactory, even though it can be eliminated in any number of ways. Extensive testing and analysis has indicated that the causal mechanisms underlying such mesh irregularities and oscillations in 2-D can be associated with: (i) time step and error control policies in the basic ODE integrator of Gear which is presently used, (ii) convergence properties of the linear solver, and (iii) limitations in the first-generation regularization functions. Intensive investigation of these factors reveal the needs in future research which are discussed below.

ODE SOLVERS FOR PDE METHODS

The current status in this task area is that most existing ODE solvers are not well-suited for ready implementation in either the MFE method or numerous other advanced PDE methods. This critical comment is, again, not intended to denigrate the impressive advances in ODE research and development during the past decade; instead, it is intended to bring a strong new focus upon the needs of PDE solution methods, in general, and more specifically upon the pressing needs of adaptive grid PDE methods which may involve large numbers of discretized equations with highly distorted grids. Large distorted grid meshes may, in turn, augur for iterative linear solvers which can solve poorly conditioned matrix equations, as will be discussed further below.

A basic difficulty with most stiff ODE software has come to the fore in the present MFE research; i.e., most ODE solver packages have been designed to accommodate many different types of classic ODE problems. By classic, one

*It is apparent that these suggested mathematical problems will have to be resolved not only for the MFE method but also for most other advanced PDE methods which may seek to solve the difficult advection-diffusion equations which frequently arise in physical problems.

refers here to such problems as chemical kinetics systems in which the dependent variables (e.g. species concentrations) are all generically the same. The error and time step controlling policies in solvers for classic ODE problems are usually less than satisfactory for applications of the ODE package to PDE solution methods. In PDE systems, the spatial dependence of generically dissimilar variables comes into play. In fluid dynamics problems, for example, the overall array of PDE variables which have been discretized on N grid nodes (x_1, x_2, \dots, x_N) can be represented as $\{\rho_1, m_1, E_1, \rho_2, m_2, E_2, \dots, \rho_N, m_N, E_N\}$, where $\rho_1 \equiv \rho(x_1)$, $\rho_2 \equiv \rho(x_2)$, etc. An ODE solver then operates on this array of discretized PDE variables as a single large vector $\{y_1, y_2, y_3, y_4, \dots, y_{3N-2}, y_{3N-1}, y_{3N}\}$, where $y_1 = \rho_1$, $y_2 = m_1$, $y_3 = E_1$, $y_4 = \rho_2$, etc. Because the error control policies in the Gear ODE package, for example, are based upon L^2 norm of all normalized quantities $y_i/(y_i)_{\max}$, unacceptably large errors can be admitted in some individual components of ρ , m , or E at arbitrary spatial locations. A much better measure for error control policies in PDE applications are maximum norms applied to each discretized PDE variable. The implementation of alternative norms is found to extend deeply into the logical structure of most ODE software packages, and alterations must usually be performed by someone who is intimately familiar with the ODE package.

In view of such considerations, we devoted significant levels of effort to: (i) modifications of Gear's basic ODE method for MFE computations; this involved wholesale alterations of the internal Gear code structure and also extensive considerations of scaling of MFE problem variables; and (ii) inevitably, the development of entirely new ODE integration procedures which better serve PDE solution needs.

The extensive modifications to Gear's method have sufficed to solve moderately challenging PDE's with modest numbers of MFE grid nodes as was seen above. But it is now clear, also, that completely new ODE code structures will be needed in pending large-scale MFE computations. We have, therefore, undertaken the development of a low-order Runge-Kutta integration package for MFE computations. This solver addresses several PDE needs: First, error control measures operate on flexibly ordered variable arrays using maximum norms on a (PDE) component-by-component basis. Second, PDE solutions have been found to require much more gradual time step advancement

policies than have been built into most classic ODE solvers.* This distinction between classic ODE and PDE time step properties apparently stems from the fundamentally coupled space-time dependences in PDE systems, vis à vis classic ODE problems which have no direct or implied spatial dependences. Whereas it is computationally worth the effort to attempt very large incremental increases (sometimes by several orders of magnitude) in Δt in classic ODE applications --even if such attempts may sometimes fail--one finds that the computational penalties for unsuccessful large Δt increases are much more severe in those PDE applications where space-time couplings augur intrinsically for more gradual Δt advancement policies. Third, time step control policies in the new ODE solver also incorporate convergence criteria from iterative linear systems solvers. Such iterative solvers should henceforth be used in largescale MFE computations in the interest of minimizing computer memory requirements. Fourth, low-order ODE methods are now used because high-order solvers provide no apparent advantages in MFE applications. Low-order methods serve to simplify the numerical logic, improve the code reliability, and avert possible errors associated with changes of order which are sometimes present in classic ODE system solvers. Finally, constraints on allowable fractional changes in PDE dependent variables are incorporated in the overall time step control policy in the new ODE solver.

LINEAR SOLVERS FOR THE MFE METHOD

Advection-diffusion equations have steadfastly resisted (if not defied) satisfactory numerical solution whenever they have been used to describe physical processes over highly disparate scales. Such problems occur, for example, in numerous applications of Navier-Stokes equations to viscous compressible fluids which may contain shear layers, shocks, and separated flows. The basic difficulty derives from the nature of the matrix equations which must be solved in numerical PDE methods that are applied to these problems. The matrix equations for discretized advection-diffusion PDE's are large, sparse linear systems in which the matrices are non-symmetric and are not necessarily dominated by large terms on the diagonal. The skewness of these PDE matrices can become quite large for large Δt 's and for highly

*These policies also extend deeply into the ODE code structure.

distorted grid meshes, both of which are key factors in efficient solutions of difficult advection-diffusion equations.

The simple advection-diffusion equation, $y_t + \underline{c} \cdot \underline{\nabla} y = \nu \nabla^2 y$, can be used to illustrate some of these features. Upon discretization of the advection-diffusion equation, a linear system of the form $(A+B)x = C$ must be solved. The matrix A represents the stencil associated with the advection operator, and the matrix B represents the stencil associated with a nine-point difference scheme for the Laplacian operator in 2-D. For representative values of Δt , these matrices may contain elements with the scaled magnitudes shown below:

$$A = \begin{pmatrix} 0 & 15 & 0 \\ -15 & 0 & 15 \\ 0 & -15 & 0 \end{pmatrix} \quad (3)$$

$$B = \begin{pmatrix} 1 & 4 & 1 \\ 4 & -20 & 4 \\ 1 & 4 & 1 \end{pmatrix}, \quad \text{and} \quad (4)$$

$$(A+B) = \begin{pmatrix} 1 & 19 & 1 \\ -11 & -20 & 19 \\ 1 & -11 & 1 \end{pmatrix}. \quad (5)$$

Testing and analysis has revealed that most available linear solvers have relatively poor rates of convergence when such significant large elements can occur away from the diagonal in non-symmetric matrices. Such iterative matrix solution methods as conjugate gradient, multi-grid and numerous other modern linear systems solvers (which may work well for symmetric matrices in discretized elliptic equations and/or for uniform grid meshes) do not converge satisfactorily in presently considered advection-diffusion problems. The source of difficulty clearly derives from the highly skewed matrices and dominant off-diagonal terms. We have also shown that the direct L-U decomposition method which has been used in the Gear method until recently becomes both noisy and computer storage limited when large bandwidths arise in problems with more than a moderate number of MFE grid nodes.

Having identified more clearly the significance of these issues, we have developed, in collaboration with Professor Keith Miller, one promising new

approach to handling more effectively these imposing PDE requirements on linear systems solvers. This new matrix solution scheme has, so far, achieved good convergence rates for Δt 's which may be 10 to 20 times greater than the large values of t called for by the ODE integrator. (It is generally hoped in PDE solutions that the time step size is determined by the truncation error of the ODE integrator and not by severely limited convergence properties of the linear solver.) This advanced linear solver has solved the Burger's equations discussed above with the same CPU cost as the direct L-U decomposition method in the Gear solver, but with greatly reduced storage requirements.

REGULARIZATION

Regularization techniques have rarely been used systematically, if at all, in PDE research in the past. There is thus presently great confusion and misunderstanding of the role of regularization techniques in PDE solution methods. On the one hand, many practitioners of conventional PDE methods suspect that regularization is an unfair trick by which one can force PDE solutions to come out in any desired manner and that such methods can therefore not be trusted. On the other hand, regularization methods are proving to be valid and powerful mathematical tools which can now be applied to achieve effective grid movement criteria systematically and to ensure that high PDE solution accuracy is also achieved in the process.

Only the simplest, first-generation regularization functions have been used in 2-D MFE problems to date. These penalty functions act like springs and/or dashpots in their action on mesh triangle altitudes (see Figure 27). The current penalty functions allow mesh triangles to distort more or less arbitrarily, so long as altitude magnitudes remain positive and maintain some designated minimum separation. This simple strategy has worked remarkably well in a surprisingly broad range of 2-D problems considered to date, and we continue to probe the limits of adequacy of this simple first-generation regularization method. In the Burger's test example discussed above with $\nu = 0.002$ and a 16 x 16 MFE mesh, minimum nodal separations were chosen to be much smaller than ν . As seen in earlier figures, the grid triangles can become very irregular and assume configurations with extremely large aspect

ratios ($O(10^2)$ to $O(10^3)$). Figures 28 and 29 below show this same Burger's test problem run with "softer" dashpot forces acting on triangle altitudes than in the run shown previously in Figure 26. The triangles in the face of the shock are more regular in this latter run, and their compaction in the center of the wavefront resolves the region where intense shearing occurs. Figure 30 shows the projection of the MFE grid mesh on the x-y plane in this example. Selected mesh connections have been traced in heavy ink in these latter figures in order to indicate the general migration pattern of the MFE nodes. It is evident that extremely large mesh triangle aspect ratios have been readily maintained near the shock front, still using the improved L-U decomposition linear solver in the modified Gear integrator in both of these runs. Perhaps more striking is the large degree of fluid shearing which is resolved in the face of this skewed shock front by the MFE grid.

In the long run, there is no fundamental reason, or desire, for the MFE mesh to always be as highly skewed as the physical flow lines in order to accurately resolve such shear layers. It was nevertheless encouraging at this stage of work that the the MFE method is able to handle such large grid aspect ratios effectively.) Alternative regularization criteria which would promote mesh homogeneity (e.g., by minimization of grid triangle aspect ratios) remain under investigation.

We have thus barely opened a potentially vast area of investigation of regularization techniques for adaptive PDE meshes. Future work should also consider highly local regularization schemes which would decrease the domain of influence of current penalty functions, particularly in view of the very attractive MFE properties which are emerging in: (i) alternative co-ordinate systems and (ii) the treatment of interface phenomena.

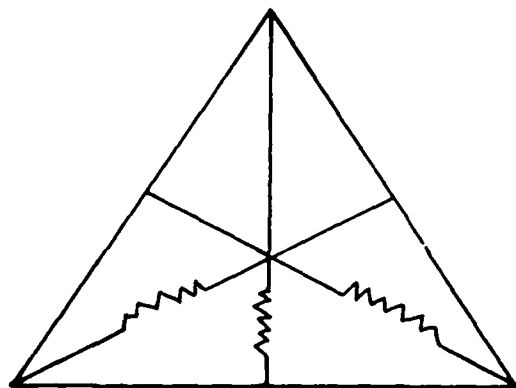
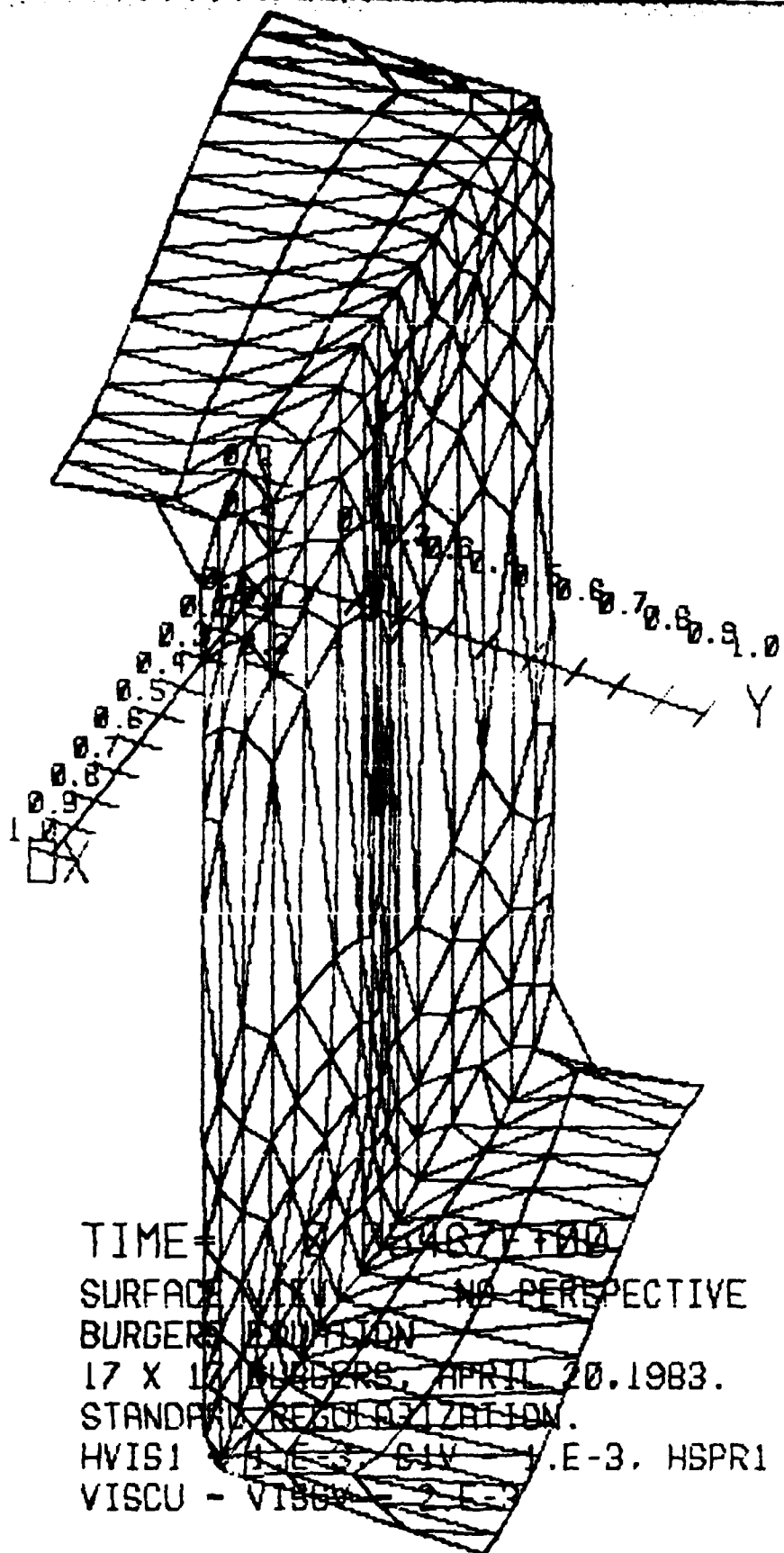


Figure 27. Schematic Representation of First-Generation MFE Regularization Functions in 2-D.



TIME = 0.487E+00
 SURFACE VIEW - NO PERSPECTIVE
 BURGERS EQUATION
 17 X 17 BURGERS, APRIL 20, 1983.
 STANDARD REGULARIZATION.
 HVISI = 1.E-3 CIV = 1.E-3, HSPR1 = 1.E-
 VISCU = VISCO = 2.E-3

Figure 28. Isometric view of the 2-D solution of the velocity
 component, v , in the Burger-like example with $v = 0.002$
 on a 16×16 MFE grid.

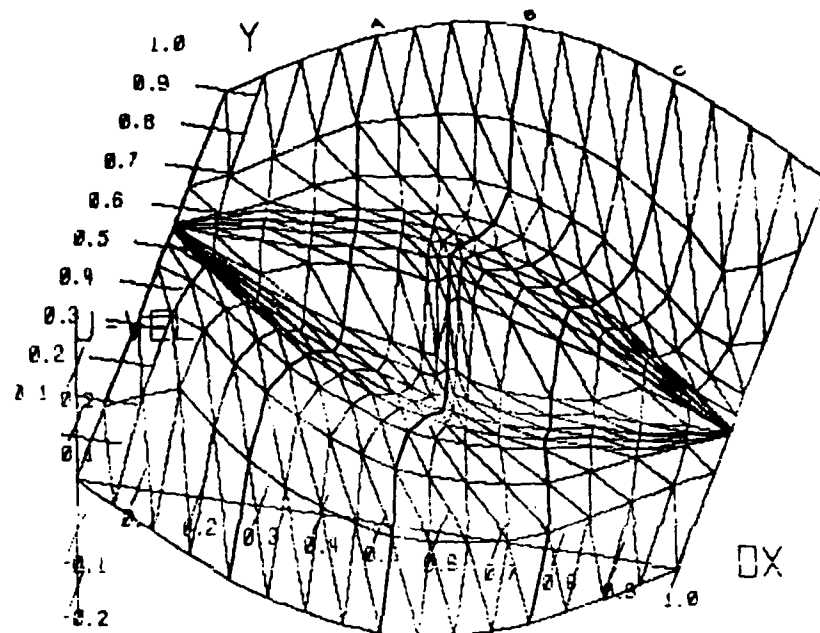


Figure 29. Isometric view of the 2-D solution of the velocity component, u , in the Burger-like example with $\nu = 0.002$ on a 16×16 MFE grid. Note that the viewing angle is rotated by 90° for a clearer view of the doubly skewed wavefront.

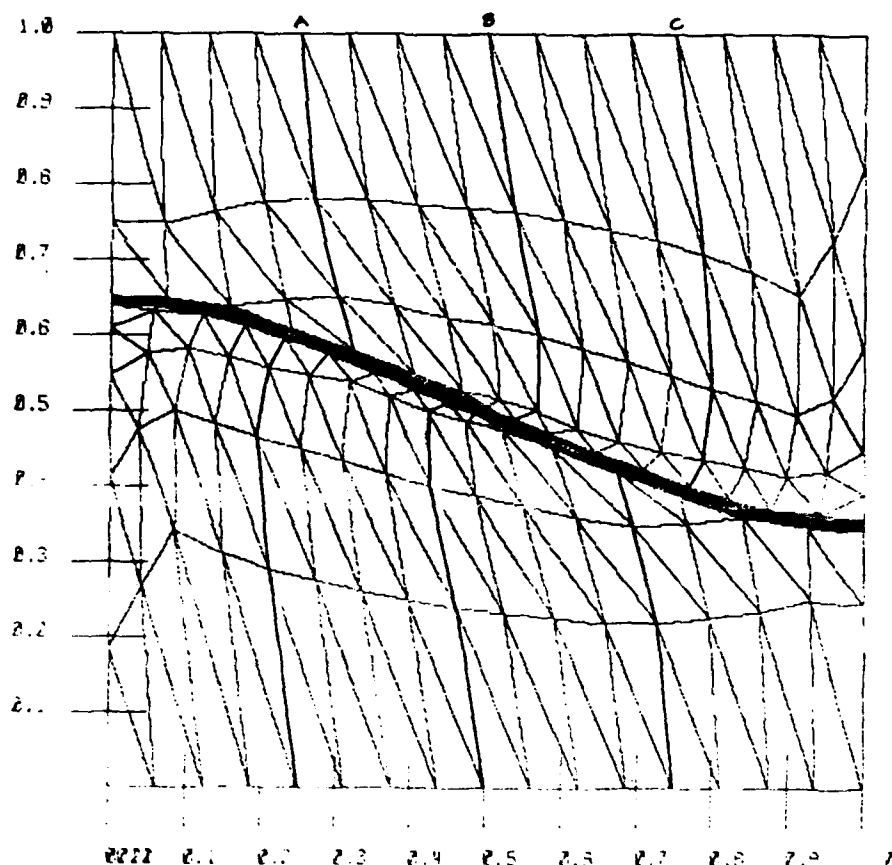


Figure 30. MFE grid projections on the x - y plane in the 2-D Burger-like example on a 16×16 grid with $\nu = 0.002$.

ALTERNATIVE CO-ORDINATE SYSTEMS

Initial work was undertaken on 2-D MFE calculations in cylindrical co-ordinates. The results in this area provide guidance for future developments in spherical co-ordinates. The apparently natural elimination of singularities at the origin by the MFE method is of major interest because such singularities have been historically troublesome in many PDE methods. For example, transport equations contain in cylindrical co-ordinates advection operators of the form $\frac{1}{r} \frac{\partial}{\partial r} (ry)$, where r is the radial co-ordinate; and y is a dependent variable of the PDE system. Singularities or other anomalous features frequently arise in discretized representations of the term (y/r) as $r \rightarrow 0$. But the MFE discretization is formulated in terms of well-defined inner products which eliminate such possible singularities. For example, the inner products of the term (y/r) with the basis function α , taken over the interval Δr , is given by

$$\int_r (y/r) \cdot \alpha \cdot r dr = \int_{\Delta r} y \cdot \alpha dr \quad . \quad (29)$$

The integral of $\alpha \cdot y \, dr$ is essentially analytic and is readily evaluated everywhere on the problem domain. This attractive MFE property in cylindrical co-ordinates obviously holds in a similar manner in spherical co-ordinates. The properties of these r -weighted norms are naturally different than the MFE inner products which were used in the Cartesian co-ordinate systems considered in earlier MFE work. Analysis and testing of these properties associated with r -weighted norms and of node controlling penalty functions in cylindrical coordinates has been limited so far, but more extensive work should continue in this area in the future.

Phase Transition Problem: A Stefan Model of a Transiently Heated Pipe Imbedded in Permafrost

In a continuing analysis of MFE node movement properties during the third year of this work, a basically cylindrical problem was considered using initially cartesian co-ordinates. This problem is solved for the transient melting of permafrost due to the presence of a heated pipe buried

within the permafrost. The material phases of ice, water, and mush are described in terms of their respective enthalpies in this Stefan model. The diagram below shows a plot of enthalpy versus temperature for the material phases of ice, water, and slush.

The variables and constants are:

h , enthalpy per unit volume	(ergs/cm ³)
T , temperature	(°K)
λ , heat capacity	(ergs/cm ³ -°K)
κ , thermal conductivity	(ergs/cm-sec-°K)
γ , latent heat of fusion	(ergs/cm ³)

The PDE for enthalpy is

$$\frac{\partial h}{\partial t} = \kappa \nabla^2 (T(h)) \quad (30)$$

This enthalpy PDE can be rewritten as

$$\frac{\partial h}{\partial t} = \left(\frac{\partial h}{\partial T} \right) \frac{\partial T}{\partial t} = \kappa \nabla^2 T \quad (31)$$

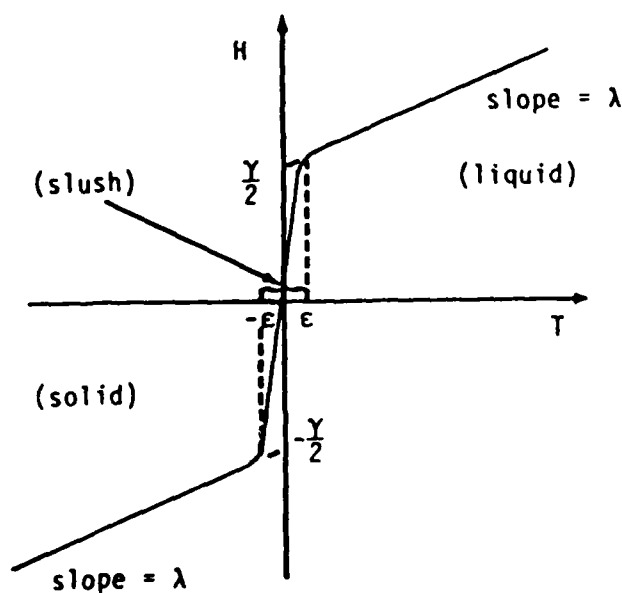


Figure 31. Diagram of Enthalpy Versus Temperature in Permafrost

The generalized heat capacity can be obtained from the diagram above. It is given by

$$C(T) \equiv \frac{\partial h}{\partial T} = \lambda + \gamma \cdot \delta(T) \quad (32)$$

where δT is a sharply peaked function. In this example

$$\delta(T) = \frac{15}{16\epsilon} [(T - \epsilon)(T + \epsilon)]^2 \quad (33)$$

Letting $\lambda = 1$, $\gamma = 2$, and $\kappa = 1$, the PDE's above become

$$[1 + 2\delta(T)] \frac{\partial T}{\partial t} = \nabla^2 T \quad (34)$$

At $t = 0$, $T = -1$. everywhere. Dirichlet conditions are maintained on the top ($y = 1$), bottom ($y = 0$), and vertical right boundary ($x = 1$). Symmetry boundary conditions apply on the vertical left boundary ($x = 0$), except at the pipe. A time-dependent Dirichlet condition,

$$T = -1 + 4 \left[1 - \frac{1}{1+t^2} \right] \quad , \quad (35)$$

describes the transient pipe temperature in the left boundary. That is, the pipe is heated from an initial temperature of -1.0 to a maximum temperature 3.0 . Figure 32 shows the original MFE grid, which is essentially Cartesian. After an initial induction period, the MFE solutions exhibit an outward, circularly propagating melt front which is, in fact, an enthalpy shock corresponding to the large gradient in enthalpy at $T = 0 \pm \epsilon$ associated with the melting phase change. Figures 33 to 35 show the ensuing evolution of this enthalpy shock using a 9×17 grid mesh.

It is interesting to note in Figures 33 and 35 that the initially Cartesian MFE grid nodes migrate readily to circular orientations before the onset of melting. After melting has begun, the MFE node contours track the

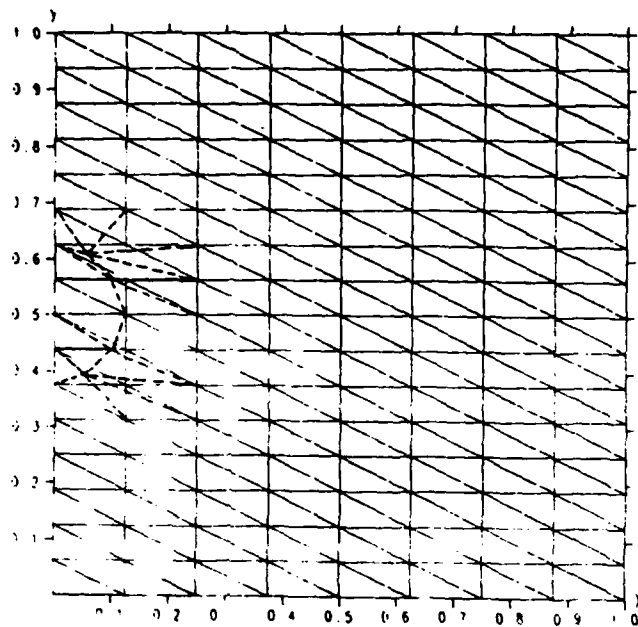
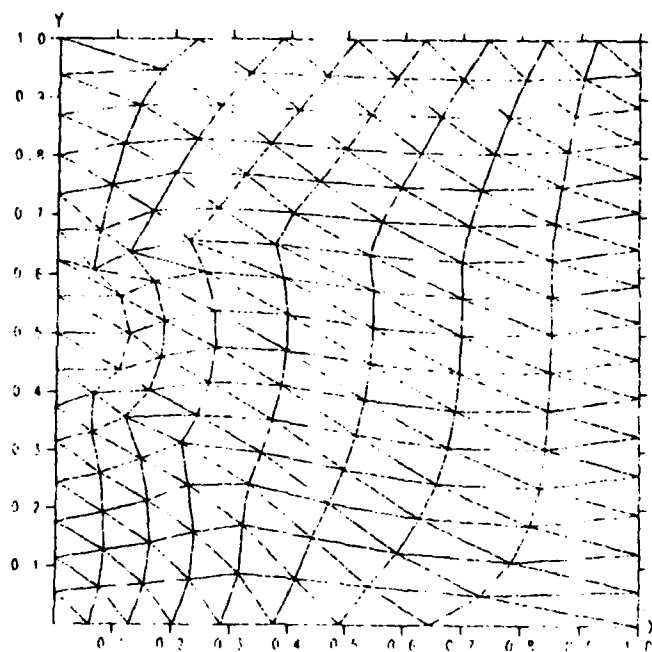


Figure 32. A 9 x 17 Node MFE Grid for Stefan Model Problem at $t = 0$. (Dotted lines denote modifications to create an initial MFE grid mesh for this problem from a standard grid mesh.)



TIME 4.000000E-01
 GRID VIEW
 STEFAN PHI
 PLT03 FEB 13 1984 5A1 RAL
 9 BY 17 STEFAN PERMATROSE PROBLEM
 MVIN1 1E-5 HSPRI 1E-08 EPS 1E-3
 CIV 0 FMB 1 KREG 2 EPSIN 0.01

Figure 33.

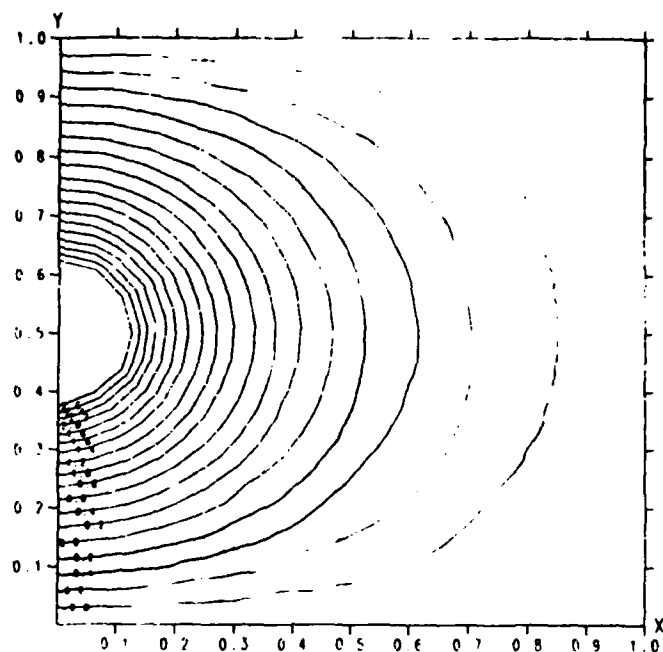


Figure 34. Temperature Contours.
Stefan Model Problem at $t = 3.0$.

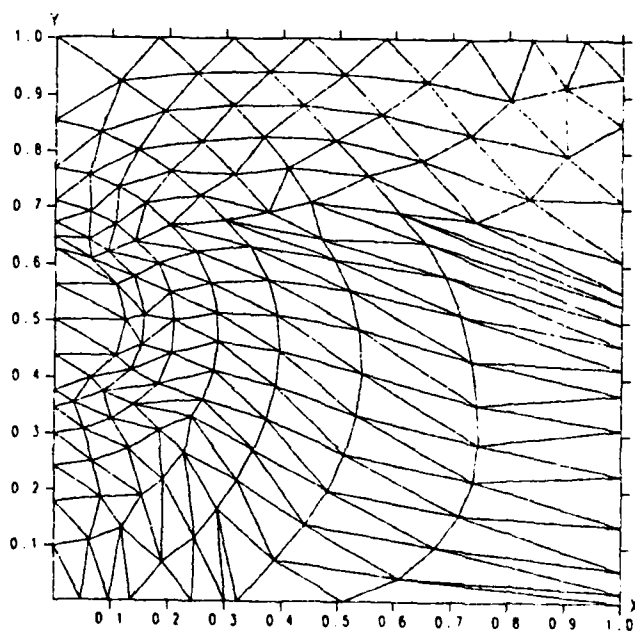


Figure 35. MFE Grid in Stefan Model
Problem at $t = 3.0$.

enthalpy shockfront curvature at $T = 0$ with high accuracy. At later times, the MFE nodes need not be strictly conformal with the shock front, per se. (See Figures 34 and 35.) High accuracies are nevertheless maintained due to the interpolation features and the residual minimization properties which are inherent in finite element formulations. Node biasing effects which are associated with the grid triangulation are also clearly evident in these results at late problem times. (See, for example, the right-hand portions of the domain; the grid pattern at the top right differs markedly from the bottom right region. It is noteworthy that very little is occurring physically in this region which contains the highest degree of grid biasing.) It is apparent that, in this particular problem, the MFE nodes exhibit a potent capacity to resolve fairly complex topological features with a small number of grid nodes, despite the presence of significant grid biasing features.

In the process of obtaining these results, the following features were observed which suggested new MFE research initiatives:

(i) The numerical conditioning of the MFE integrations can become poorly conditioned in difficult, highly complex flow regimes. Numerous possible causes and remedies which should be investigated include: (i) improperly posed or incomplete physical/mathematical models; (ii) highly sheared grid cells; (iii) implicit coupling of incommensurate PDE dependent variables which can give rise to poorly conditioned, non-symmetric matrices which are devoid of diagonally dominant elements; (iv) complex flow configurations near boundaries; and (v) non-optimal regularization.

(ii) The simple grid triangle connection scheme which is used in this example (with all grid diagonals having the same orientation) can exhibit a distinctive biasing effect in the evolving MFE mesh orientations. In many problems such grid biasing is of no practical consequence. For example, MFE solutions of planar wavefronts maintain extremely high accuracies despite transverse grid biases.) In other large-gradient problems, grid biasing has been found to: (i) hamper computational efficiency, and (ii) possibly impair numerical conditioning and accuracy. Several alternative grid connection schemes are logical candidates for testing and implementation in order to improve, and

possibly eliminate, such grid biasing effects. Alternative regularization methods are also beginning to show some promise.

(iii) Matrix solvers. Extensive testing of matrix solvers for fully implicit MFE calculations indicated three general size distinctions in the choice of matrix solvers for use on CRAY-capacity computers; these are:

- Small problems; e.g., gas dynamics equations -- which are discussed in the next sample problem -- for the dependent variables ρ , u , v , E , x , and y on a 10×20 grid mesh, or smaller. Direct L-U decomposition methods can be, and have been, used quite effectively in small problems. Other small problems include Burger's equations on a 25×25 mesh, as described above.
- Medium problems; e.g., gas dynamics on a 30×30 grid mesh. Various iterative multigrid methods exhibit some promise in this size range. Additional research, development, and implementation is very much in order here.
- Large problems are defined by default from the items immediately above. Practical solutions of large problems are an ultimate objective for applications of the MFE method. Advanced iterative solvers, including perhaps dynamic ADI and/or other equation-splitting alternatives remain to be investigated in conjunction with both medium and large problems.

Gas Dynamics Problems Which Address Physical versus Non Physical (Numerical) Dissipation Effects in Gases

It is well known in aerodynamics that shockwave-boundary layer interactions are dependent upon local viscous dissipation and thermal conduction processes for the distribution of internal and kinetic energies. This dependence can in many applications be a sensitive determinate of macroscopic flow properties. Such shock-boundary/shear layer processes can impose severe

demands upon computer codes because the most reliable computations of the essential physical processes must first include the physical dissipation operators of the full Navier-Stokes equations and then use optimally distributed grid densities which can accurately resolve the actual physical dissipation processes and eliminate the numerical dissipation processes. To gain a full appreciation of the origin and nature of physical dissipation processes, it is well to recall the development of the Navier-Stokes equations in the context of 1-D kinetic theory. That is, the fluid equations can be written as:

$$\frac{\partial \rho}{\partial t} + \frac{\partial}{\partial x} (\rho v) = 0 \quad (36)$$

$$\frac{\partial (\rho v)}{\partial t} + \frac{\partial}{\partial x} (\rho v^2) = - \frac{\partial}{\partial x} p^{(0)} + p^{(1)} + p^{(2)} + \dots \quad (37)$$

$$\frac{\partial E}{\partial t} + \frac{\partial}{\partial x} (E v) = - \frac{\partial}{\partial x} (p v) - \frac{\partial}{\partial x} q^{(0)} + q^{(1)} + q^{(2)} + \dots \quad (38)$$

A zero-th approximation of the kinetic theory for gases uses the constitutive relations for an inviscid, non-conducting fluid; i.e.,

$$p = p^{(0)} = \frac{\rho R T}{A} = (\gamma - 1) \left(E - \frac{1}{2} \rho v^2 \right) \quad (39)$$

$$q = q^{(0)} = 0 \quad (40)$$

These relationships yield the well-known, inviscid Euler equations.

A first approximation of the kinetic theory for gases gives the Navier-Stokes equations according to:

$$p = p^{(0)} + p^{(1)} = (\gamma - 1) \left(E - \frac{1}{2} \rho v^2 \right) + \frac{4}{3} \mu \frac{\partial v}{\partial x} \quad (41)$$

$$q = q^{(0)} + q^{(1)} = - \kappa \frac{\partial T}{\partial x} \quad (42)$$

A second approximation of kinetic theory gives the Burnett equations, etc.

In order to address the primary issue of the potential significance of physical dissipation processes as determinates of transient macroscopic flow properties, we wish to distinguish the relative roles in code calculations of numerical vis à vis the physical dissipation effects which appear on the right hand sides of Equations (37) and (38). For this, we have solved a simple shock-boundary layer reflection process in 1-D. This example is frequently referred to as the anomalous wall heating problem.⁽⁹⁾ In this problem, anomalously high temperatures are calculated by many existing shock hydrodynamics codes for the reflection of a planar shock from an infinitely reflecting wall in slab geometry. The MFE results which follow indicate that the anomalous aspects are eliminated when numerical dissipation is suppressed and, most importantly, when the physical dissipation processes in the Navier-Stokes equations are accurately resolved in the transient reflection process. The following test problem in 1-D slab geometry illustrates these results:

Initial Conditions:

$$\begin{array}{ll}
 (x, 0) = 1 & 0. \leq x \leq 2. \\
 p(x, 0) = e(x, 0) = 0 & 0. \leq x \leq 2.0 \\
 v(x, 0) = -1 & \Delta x_0 \leq x \leq 2.0 \\
 v(x, 0) = \text{linear} & 0 \leq x \leq \Delta x_0 \\
 v(x, 0) = 0 & x = 0. \\
 \gamma = 5/3 &
 \end{array}$$

Boundary Conditions:

Reflection at $x = 0$.
 Dirichlet at initial values at $x = 2.0$

Rankine-Hugoniot Solutions for Infinite Shock ($t \rightarrow \infty$):

$$\begin{array}{ll}
 s = 1/3 & \\
 \rho^+ = 4.0 & ; \quad \rho^- = 1.0 \\
 e^+ = 0.5 & ; \quad e^- = 0. \\
 v^+ = 0. & ; \quad v^- = -1. \\
 p^+ = 1.33 & ; \quad p^- = 0.
 \end{array}$$

The time evolution of this shock was solved by the MFE method in two ways: First the full Navier-Stokes equations were solved accurately using alternative values of $\nu = 4\mu/3$ and κ . These solutions are denoted by N-S in the accompanying figures. In one set of N-S solutions, $\nu = \kappa = 0.01$, which is unrealistically large but which permits comparisons to other fixed node

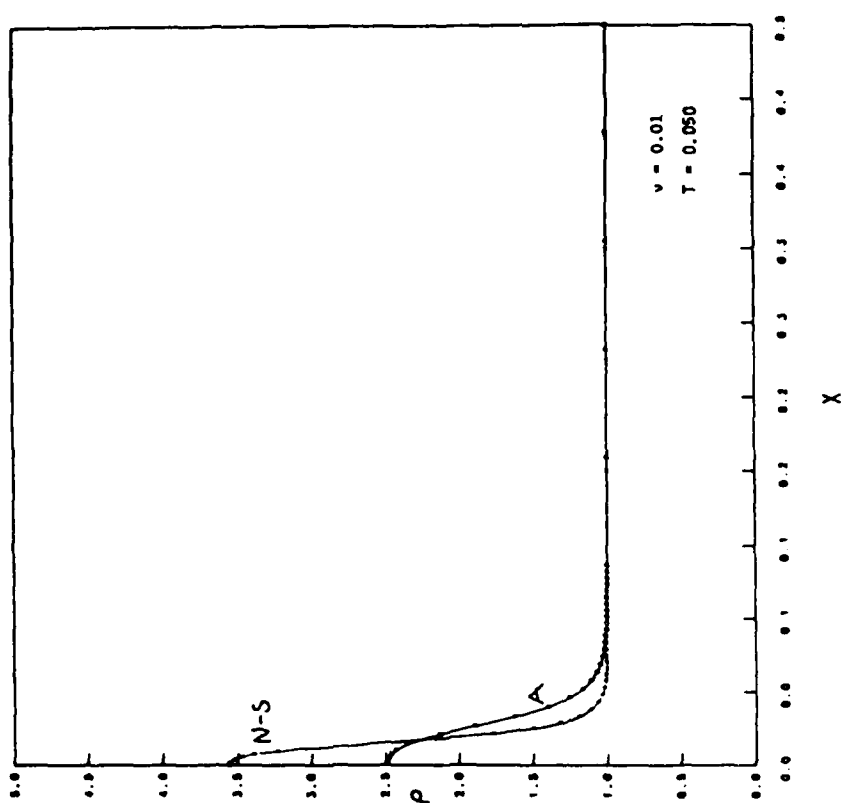


Figure 36. MFE solutions of the Navier-Stokes equations and anomalously dissipative equations at time = 0.050.

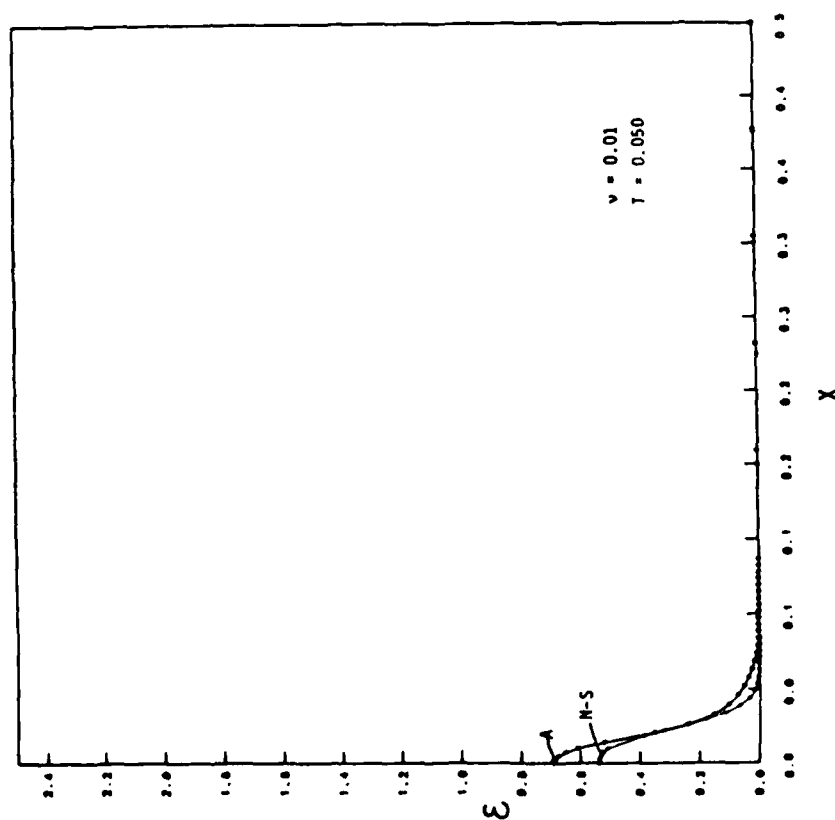


Figure 37. MFE solutions of the Navier-Stokes equations and anomalously dissipative equations at time = 0.050.

PDE solutions that may use on the order of 100 to several hundred grid nodes. In another set of N-S solutions, $\nu = \kappa = 0.001$, which approximates physically realistic values for actual dissipation processes in gases. Second, the variable ϵ denotes internal energy per unit mass in the accompanying figures, and anomalous diffusion (denoted by A in the accompanying figures) was simulated by including a diffusion term $\nu_r \rho_{xx}$ in Equation (36). This effectively simulates some form of uncontrolled numerical diffusion which is present intrinsically in all numerical PDE solution methods. (Uncontrolled numerical diffusion is the only source of dissipation in numerical solutions of the inviscid Euler equations.) In the results which follow, we have verified that the MFE solutions of the Navier-Stokes equations have reduced all numerical or other anomalous diffusion effects to imperceptible low levels and that the observed behavior of shock interactions is associated with physical dissipation operators.

At $t = 0_+$, the shock incident on the origin is in the incipient state of outward reflection. At $t = 0.05$, Figures 36 and 37 show that the calculations of the reflected shock with uncontrolled diffusion (or simulated numerical diffusion) tend immediately to overheat in ϵ and to correspondingly under-shoot in p relative to the Navier-Stokes solutions. Although these transient solutions are not near their steady state values at this early time, it will be seen that the ensuing evolution toward equilibrium is quite sensitive to both the magnitudes and the nature of the dissipation processes in the computations.

Figure 38 shows that at $t = 0.15$, the lip of the shock in the Navier-Stokes solution is approaching the steady state value of $\rho = 4.0$, and the anomalous dissipation solution lags by a significant margin. The fluid buildup at the front of the shock is evident here because the fluid near the origin has stagnated while additional fluid continues to stream in toward the origin from the region to the right of the shock. Figure 39 shows that the anomalous dissipation results continue to lag behind the Navier-Stokes solutions to a significant degree at $t = 0.300$. At $t = 2.0$, the Navier-Stokes solutions have approached steady state Rankine-Hugoniot conditions (not shown in Figure 40), and the anomalous dissipation solution has still not reached the Rankine-Hugoniot values in the vicinity of the origin. The anomalous

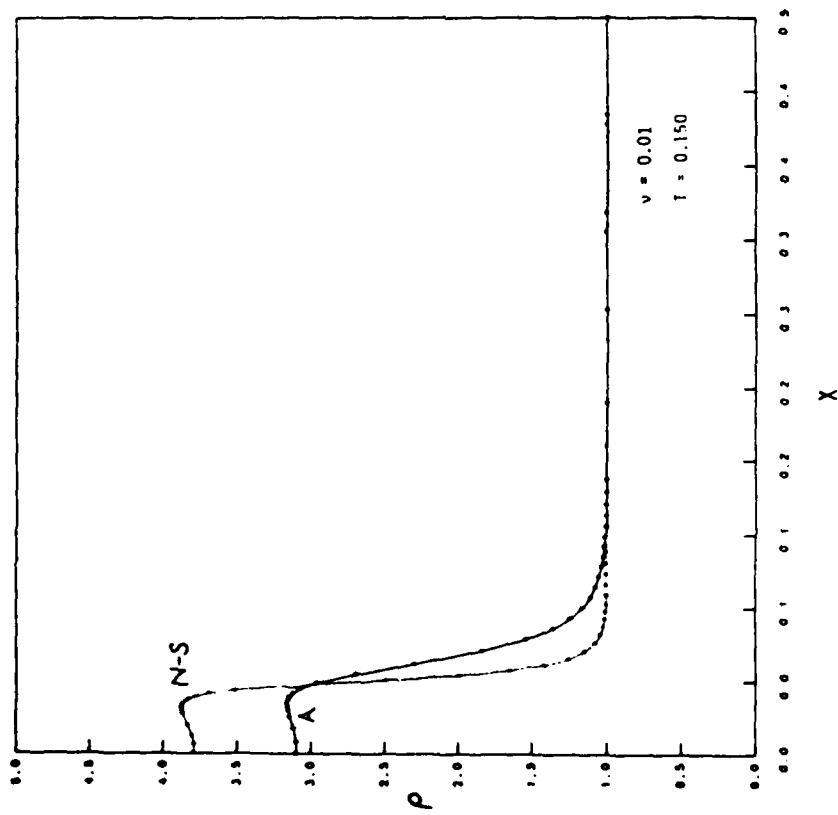


Figure 38. MFE solutions of the Navier-Stokes equations and anomalously dissipative equations at time = 0.150.

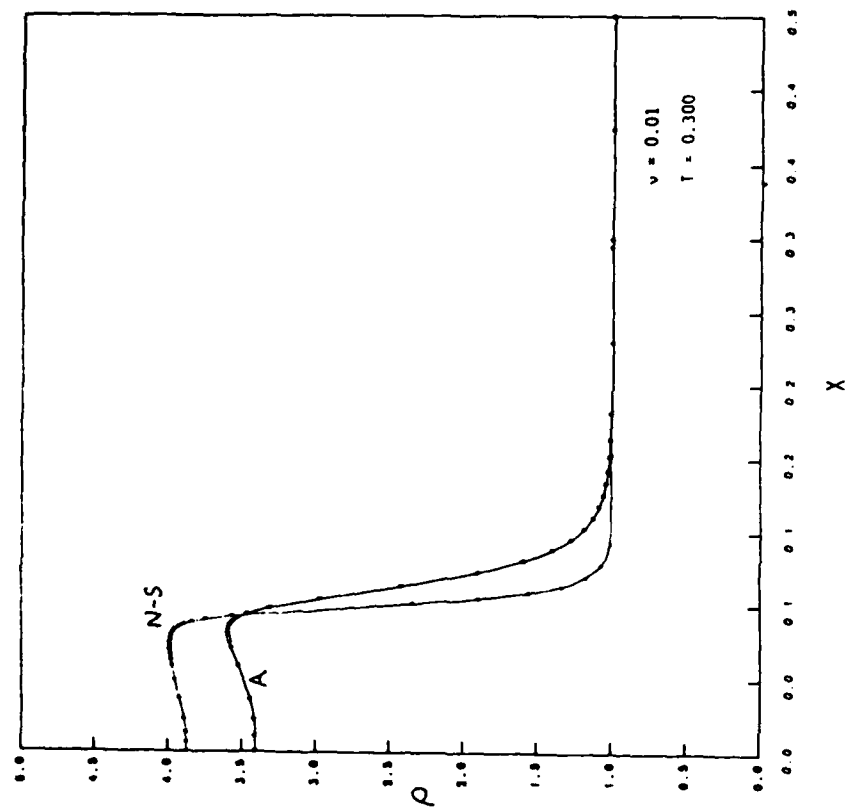


Figure 39. MFE solutions of the Navier-Stokes equations and anomalously dissipative equations at time = 0.300.

wall heating effects due to uncontrolled dissipation in the density equation have thus persisted to very long times vis à vis the accurate solutions of the Navier-Stokes equations. Non-physical dissipation which is sometimes introduced as artificial viscosity terms in fluid calculations can be shown to have similar anomalous effects, as can the numerical dissipation and/or numerical uncertainties which are present in solvers of inviscid Euler equations.

Figures 41 and 42 present the results of another test of sensitivity of the Navier-Stokes solutions to non-optimal grid locations. In this test problem, a physically realistic value of $\nu = 0.0001$ is used in MFE solutions of the Navier-Stokes equations. We have, however, deliberately constrained the MFE grid nodes in this test case so that they do not migrate to their truly optimal locations, as in the results considered previously. Figure 41 shows several significant features: (i) the shock gradients associated with $\nu = 0.0001$ are extremely large; the accurate resolution of these gradients would require several thousand nodes if a fixed node PDE solution method were to be used, (ii) the Rankine-Hugoniot solutions are approached much more rapidly for the physically realistic values of ν than for the larger values of ν which are typically used either tacitly or explicitly in many other PDE solution methods, and (iii) the slight constraint on node movements and thus on nodal positions do not show up immediately; but once the perturbation becomes significant (as seen in Figure 42), its effects can grow rapidly. In summary, these results demonstrate that reflected shock solutions can be very sensitive to non-physical dissipation effects and to slight deviations from optimal grid node positioning, even in adaptive gridding methods. All of the results in this section were obtained with approximately 30 MFE nodes. As many as 61 MFE nodes were used to verify that the MFE solutions were in fact converged solutions. We have also compared the steady state MFE solutions of fluid velocities with the analytic Navier-Stokes solutions of the steady shock. Excellent agreement was obtained between the MFE solution and the analytic Navier-Stoke solution. In contrast, it was found after extensive attempts that computed solutions which contained nominal degrees of numerical or other anomalous diffusion could not be forced by parameter manipulations to agree with the analytical shock solutions. In still other MFE calculations, we have computed in 1-D the interaction of a shock with an internal

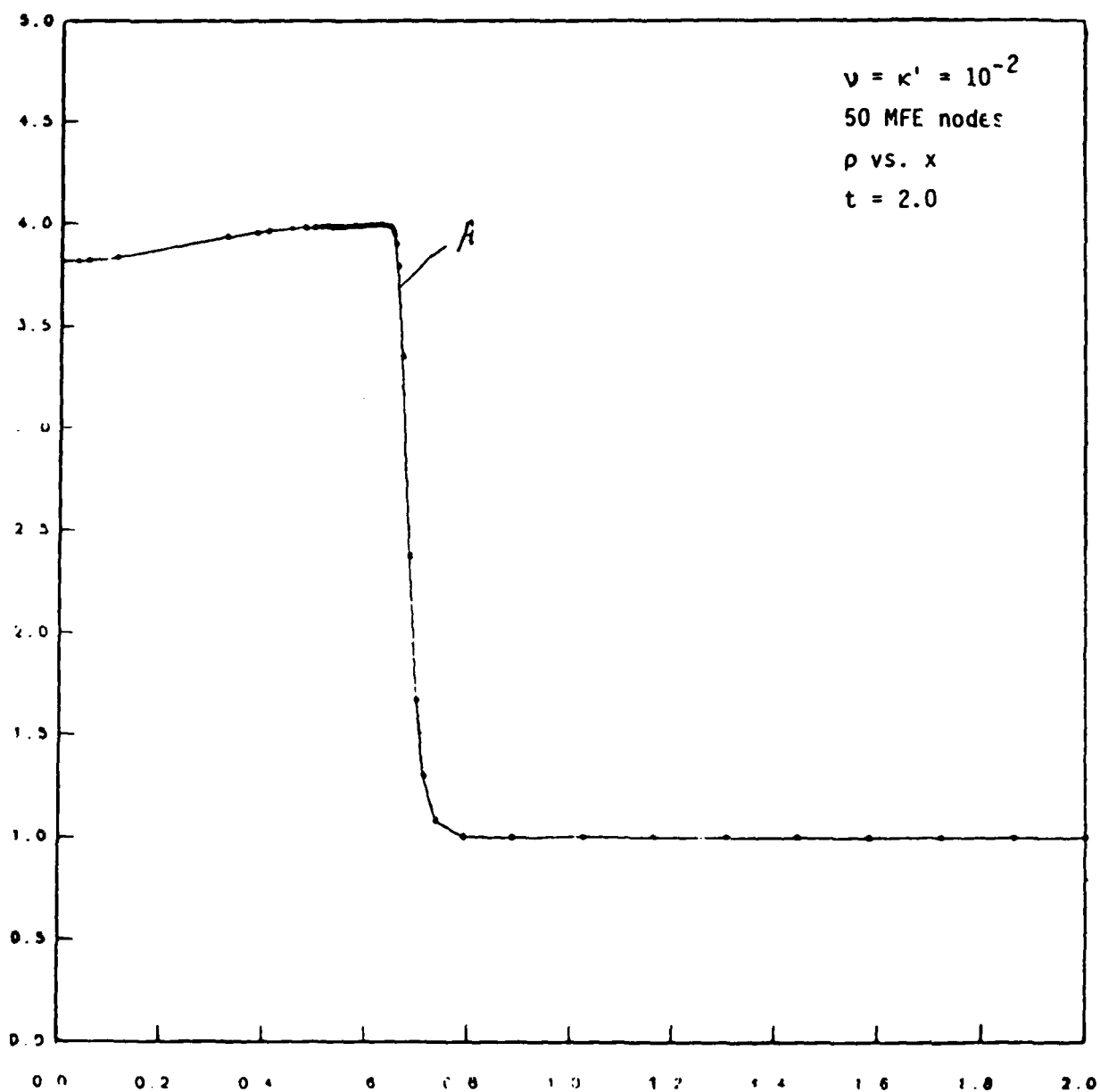


Figure 40. MFE solutions of the Navier-Stokes Equations and anomalously dissipative equations at time = 2.0.

N-S

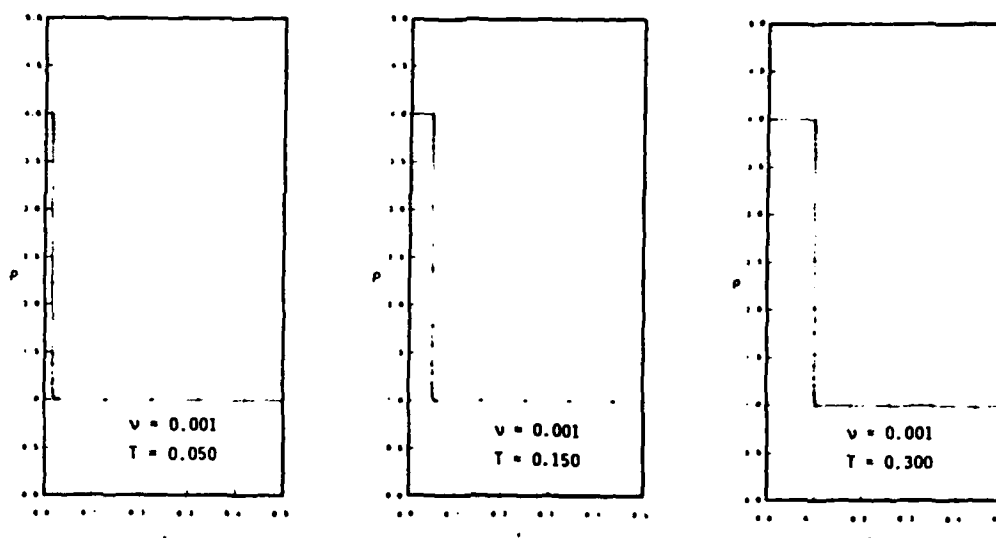


Figure 41. MFE solutions of Navier-Stokes equations with some deliberately constrained grid nodes.

N-S

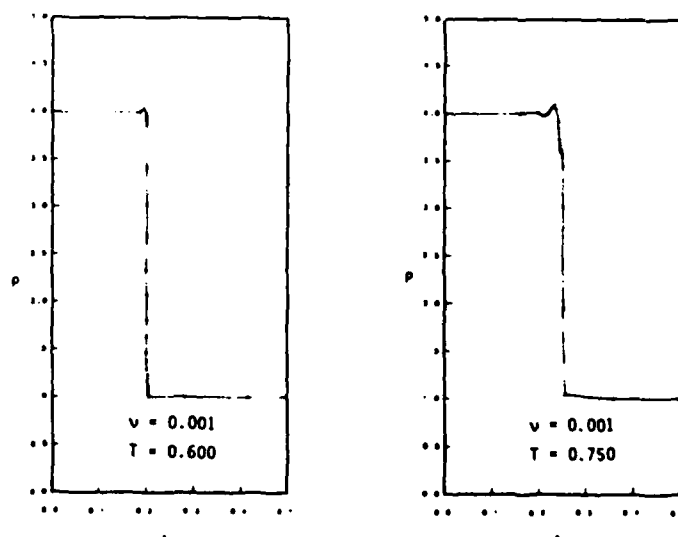


Figure 42. MFE solutions of Navier-Stokes equations with some deliberately constrained grid nodes.

shear layer associated with a contact discontinuity -- in direct analogy to the irregular shock reflection mechanisms which occur in higher dimensions. Here also, the computed macroscopic flow properties were sensitive to accurate resolution of the physical dissipation processes in the full Navier-Stokes equations. In the absence of the stringent tests of convergence which were applied here, it can be extremely difficult to discern physical oscillations and dissipation effects from non-physical and/or purely numerical oscillations and dissipation effects. We have, in fact, found it generally impossible to simulate the effects of the actual physical dissipation processes in shock-boundary layer interactions by the use of either artificial or parametrically controlled numerical diffusion processes in Euler equation solutions.

Shock-on-Wedge Problem in 2-D

A shock-on-wedge problem which can be verified against the experimental data of Glass and co-workers⁽¹⁰⁾ has been addressed in 2-D MFE calculations. This problem is posed in rectangular coordinates, as shown by the schematic view of an initial grid mesh configuration in Figure 43.

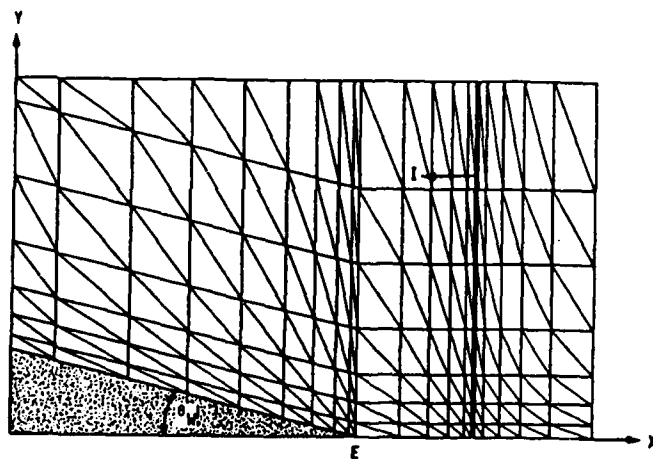


Figure 43. MFE Initial Grid Zone Configurations for Shock-on-Wedge Problems.

In 2-D, we have used the mass, momentum, total energy representation (ρ , \underline{m} , E) of the fluid equations. The Navier-Stokes equations in the (ρ , \underline{m} , E) representation are given by

$$\frac{\partial}{\partial t} + \underline{\nabla} \cdot \underline{m} = 0 \quad (43)$$

$$\frac{\partial \underline{m}}{\partial t} + \underline{\nabla} \cdot (\underline{m} \underline{m} / \rho) = \underline{\Sigma} \cdot \quad (44)$$

$$\frac{\partial E}{\partial t} + \underline{\nabla} \cdot (E \underline{m} / \rho) = -\underline{\nabla} \cdot \underline{Q} + \underline{\nabla} \cdot (\underline{\Sigma} \cdot (\underline{m} / \rho)) \quad (45)$$

where $\underline{\Sigma}$ is the generalized stress tensor and \underline{Q} is the heat flux vector. The heat flux vector is frequently given by

$$\underline{Q} = -\kappa \underline{\nabla} T \quad (46)$$

where T is the temperature. The general stress tensor is frequently given by

$$\underline{\Sigma} = -p \underline{I} + \underline{\tau} \quad (47)$$

where \underline{I} is the identity matrix. For an ideal gas (a Newtonian fluid) in Cartesian co-ordinates

$$p = p^{(0)} = (\gamma - 1)(E - m^2/2\rho), \text{ and} \quad (48)$$

$$\tau_{xx} = 2\mu \frac{\partial(\underline{m}/\rho)_x}{\partial x} - \frac{2}{3}\mu (\underline{\nabla} \cdot (\underline{m}/\rho)) \quad (49)$$

$$\tau_{yy} = 2\mu \frac{\partial(\underline{m}/\rho)_y}{\partial y} - \frac{2}{3}\mu (\underline{\nabla} \cdot (\underline{m}/\rho)) \quad (50)$$

$$\tau_{xy} = \mu \left[\frac{\partial(\underline{m}/\rho)_x}{\partial y} + \frac{\partial(\underline{m}/\rho)_y}{\partial x} \right] \quad (51)$$

It is important to note in Equation (44) that the quantity $\underline{m} \underline{m}$ is a dyadic. Special attention has been devoted to exacting evaluations of those inner product terms which involve factors of $\frac{1}{\rho}$ for small ρ . These factors are present in all standard representations of the fluid equations.

This 2-D test problem considers the case of regular shock reflection in argon at Mach number $M_S = 2.05$, $p_0 = 150$ torr, $\rho_0 = 3.23 \times 10^{-4}$ g/cm³, $T_0 = 297.6^\circ\text{K}$, and wedge angle $\theta_w = 60^\circ$ (see Figure 44).

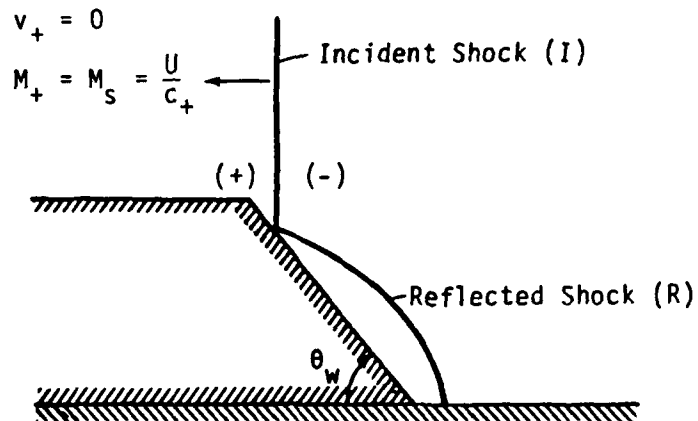


Figure 44. Schematic representation of regular reflection in Shock-on-wedge experiments.

Initial conditions calculated from the Rankine-Hugoniot relationships are:

$$\rho_+ = 3.23 \times 10^{-4} \text{ g/cm}^3$$

$$m_+ = 0$$

$$E_+ = [\rho_+ \epsilon_+ + m_+^2/2\rho_+] = 3.0 \times 10^5 \text{ ergs/cm}^3 \text{ and}$$

$$\rho_- = 7.87 \times 10^{-4} \text{ g/cm}^3$$

$$m_- = 30.559 \text{ gm - cm/sec}$$

$$E_- = [\rho_- \epsilon_- + m_-^2/2\rho_-] = 2.132 \times 10^6 \text{ ergs/cm}^3$$

Boundary Conditions

A significant point of fundamental physics became manifest in the study of boundary conditions for shock-on-wedge calculations. For a variety of reasons, conventional shock codes tend to use slip-type boundary conditions. In actuality, the velocity of air molecules is zero at the types of surfaces

under present consideration. For the sake of common comparisons, and to test the sensitivity of MFE shock-on-wedge computations to alternative boundary conditions, we first attempted to solve the regular shock-on-wedge test problem with slip-type boundary conditions, in which the normal component of velocity along the bottom horizontal surface and inclined wedge are zero and the tangential velocity components are treated by zero-Neumann (or symmetry) conditions (see Figure 44). These symmetry boundary conditions are applied similarly to the MFE grid nodes so that the grid nodes would slide freely along both the horizontal surface and the inclined wedge surface. But the MFE method has always been found to be extremely sensitive in its accuracy and consistency requirements to the presence of any physical or mathematically ill-posed condition. Here, the surface normal is not defined uniquely at the front of the wedge. Consequently, the basic consistency requirements in the MFE method impeded the numerical integration process because the symmetry boundary condition at the foot of the wedge is ill-posed, and thus could not be properly resolved as a truly rigorous PDE solution. The MFE method also tends to be less tolerant than most PDE methods of computational swindles which are frequently used to accomplish slip-type boundary conditions. It thus became quite apparent that it is possible to enforce slip-type boundary conditions only by accepting erroneous numerical solutions in the boundary layer region near the front corner of the wedge. It was further apparent that these errors could propagate to regions well away from the local source of difficulty. In view of these results, we next attempted to take a large step forward in terms of both the physics and computations of the physically required non-slip boundary conditions. This turned out to be a large step because this shock-on-wedge problem has a turbulent boundary layer in the duct represented by our problem domain. Nevertheless, some key points became manifest in this task which will be described immediately below.

The initial shock conditions are shown in Figure 45. This problem is solved in a 1 cm duct. For viscosity $\mu = 5 \times 10^{-4}$, the Reynolds number is approximately 5.7×10^4 . Such a flow is clearly turbulent. The MFE solutions of the laminar Navier-Stokes equations were nevertheless attempted as a numerical experiment. These results appear in Figures 46 to 55 with self-explanatory captions. At $t = 0.30$ the shock is just starting to encounter the wedge front; and the isodensity contours early in the reflection process

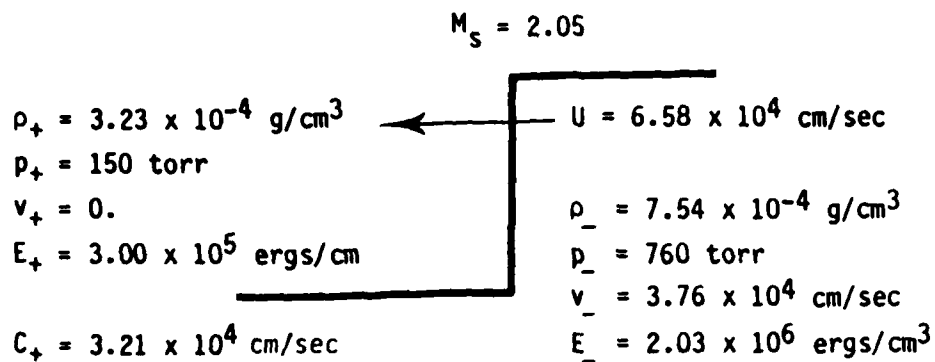


Figure 45. Initial Conditions for Regular Reflection of Planar Shock in the Experiments of Deschambault and Glass.⁽¹⁰⁾

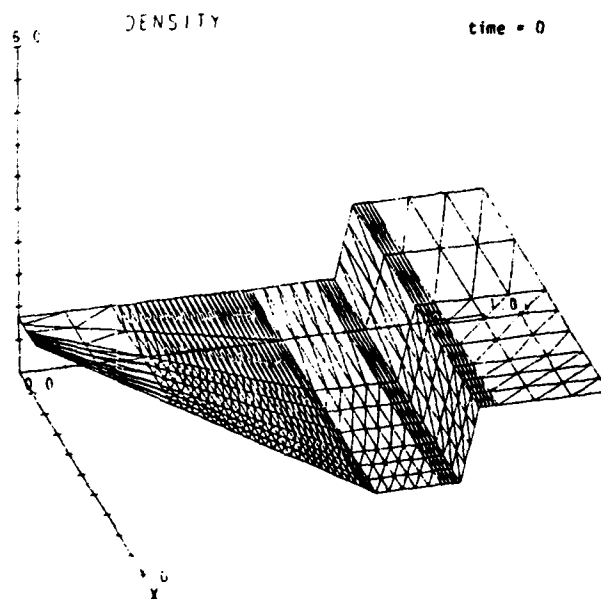


Figure 46. MFE Solutions of Laminar Navier-Stokes Equations for a Regular Shock Reflection Experiment of Deschambault and Glass. ($M_s = 2.05$, $\theta = 60^\circ$, $p_+ = 150 \text{ torr}$, $\rho_+ = 3.23 \times 10^{-4} \text{ g/cm}^3$ in Argon.) The MFE Grid is 9×51 Nodes and Non-Slip Boundary Conditions are Used.

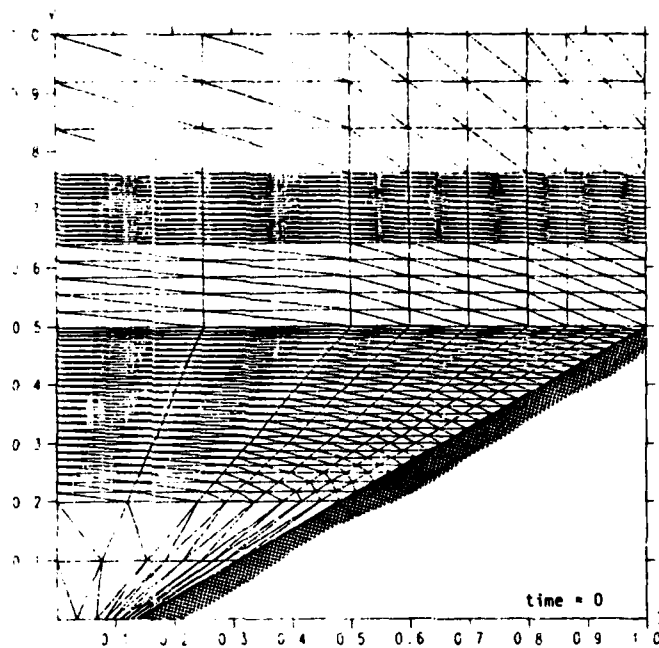


Figure 47.

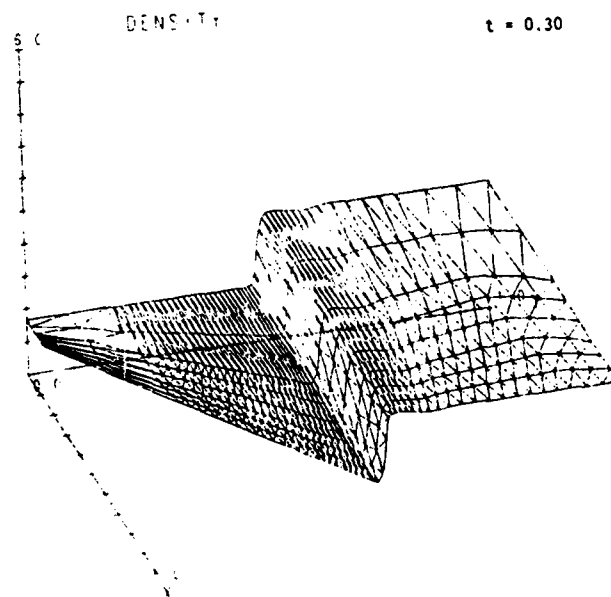


Figure 48.

MFE Solutions of Laminar Navier-Stokes Equations for a Regular Shock Reflection Experiment of Deschambault and Glass. ($M_s = 2.05$, $\theta = 60^\circ$, $p_+ = 150$ torr, $p_+ = 3.23 \times 10^{-4} \text{g/cm}^3$ in Argon.) The MFE Grid is 9×51 Nodes and Non-Slip Boundary Conditions are Used.

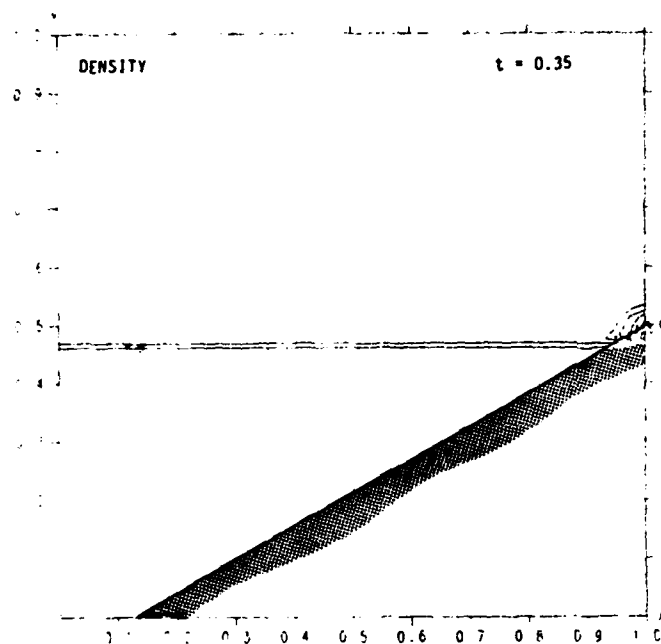


Figure 49.

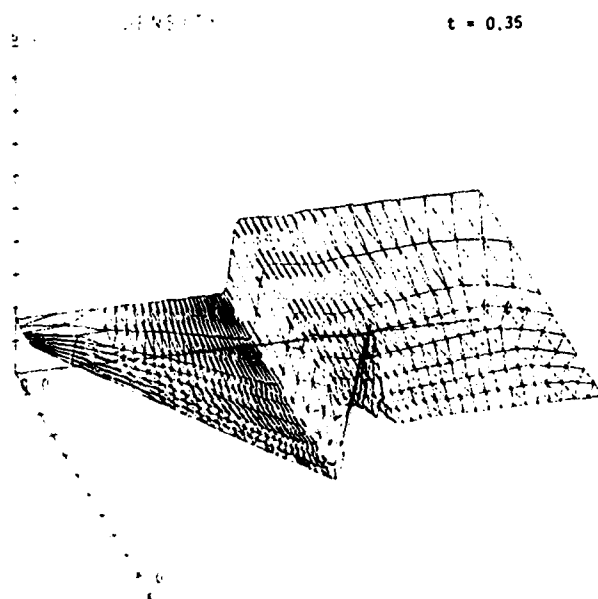


Figure 50.

MFE Solutions of Laminar Navier-Stokes Equations for a Regular Shock Reflection Experiment of Deschambault and Glass. ($M_s = 2.05$, $\theta = 60^\circ$, $p_+ = 150$ torr, $p_+ = 3.23 \times 10^{-4} \text{g/cm}^3$ in Argon.) The MFE Grid is 9×51 Nodes and Non-Slip Boundary Conditions are Used.

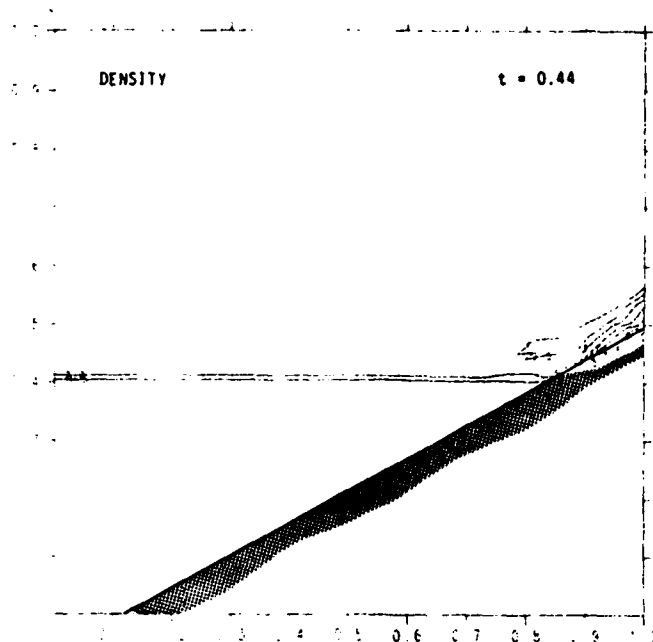


Figure 51.

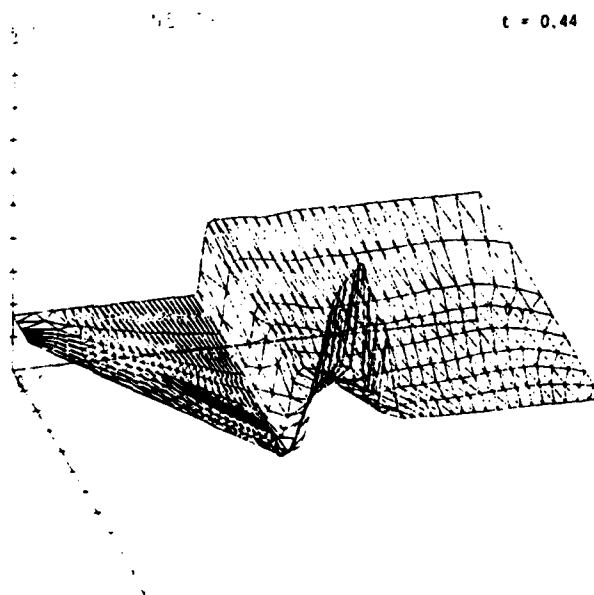


Figure 52.

MFE Solutions of Laminar Navier-Stokes Equations for a Regular Shock Reflection Experiment of Deschambault and Glass. ($M_s = 2.05$, $\theta = 60^\circ$, $p_+ = 150$ torr, $p_- = 3.23 \times 10^{-4}$ g/cm³ in Argon.) The MFE Grid is 9×51 Nodes and Non-Slip Boundary Conditions are Used.

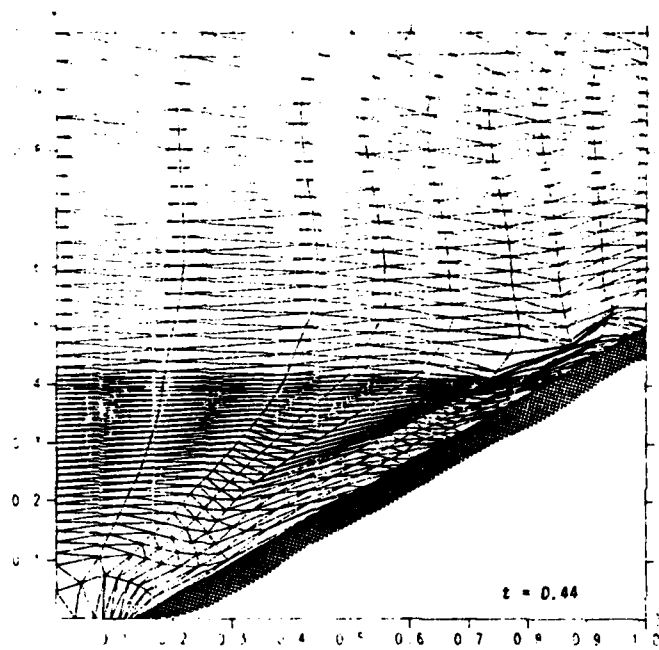


Figure 53.

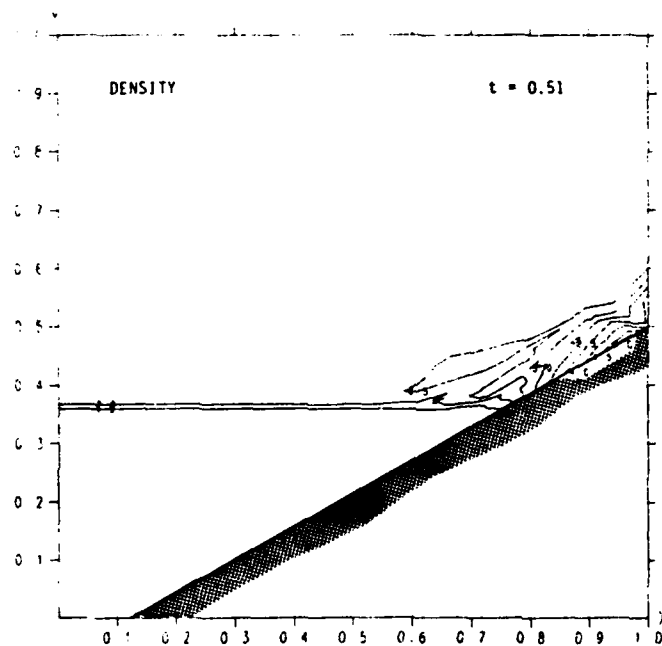


Figure 54.

MFE Solutions of Laminar Navier-Stokes Equations for a Regular Shock Reflection Experiment of Deschambault and Glass. ($M_s = 2.05$, $\theta = 60^\circ$, $p_+ = 150$ torr, $p_- = 3.23 \times 10^{-4} \text{g/cm}^3$ in Argon.) The MFE Grid is 9×51 Nodes and Non-Slip Boundary Conditions are Used.

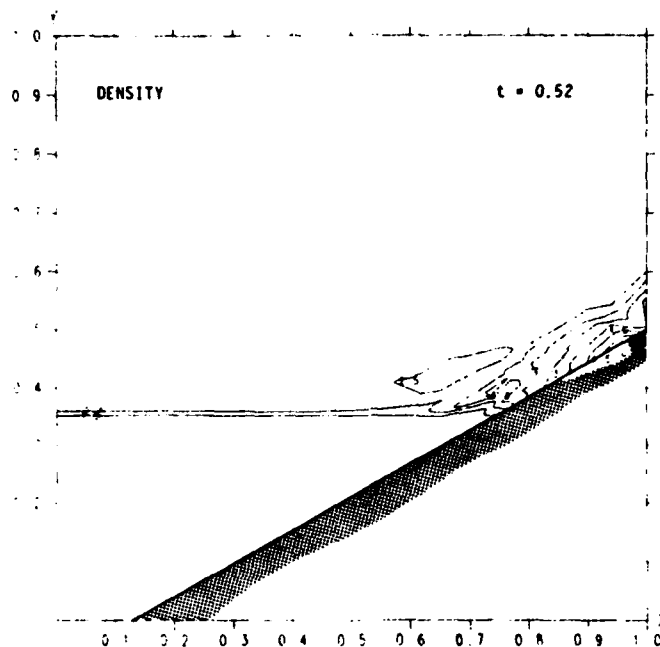


Figure 55. MFE Solutions of Laminar Navier-Stokes Equations for a Regular Shock Reflection Experiment of Deschambault and Glass. ($M_s = 3.06$, $\theta = 60^\circ$, $p_+ = 150$ torr, $\rho_+ = 3.23 \times 10^{-4} \text{ g/cm}^3$ in Argon.) The MFE Grid is 9×51 Nodes and Non-Slip Boundary Conditions are Used.

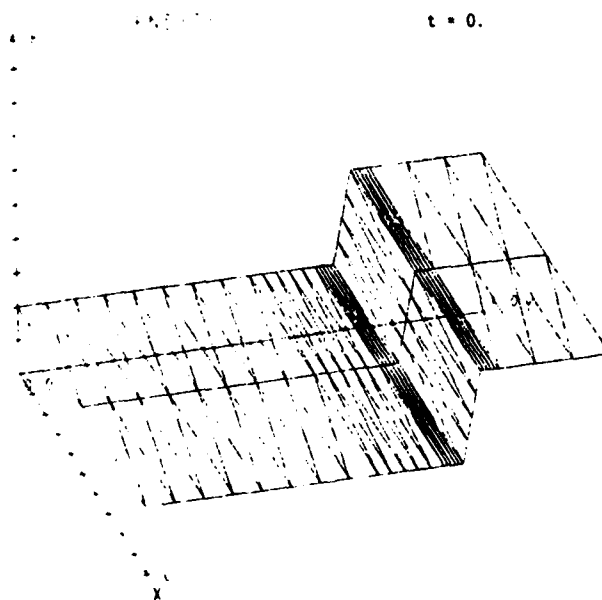


Figure 56. MFE Solutions of Laminar Navier-Stokes Equations for an Experimental Plane Shock of Deschambault and Glass Reflecting Against a Vertical Wall. ($M_s = 2.05$, $\theta = 90^\circ$, $p_+ = 150$ torr, $\rho_+ = 3.23 \times 10^{-4} \text{ g/cm}^3$ in Argon.) A 3×31 MFE Grid is Used.

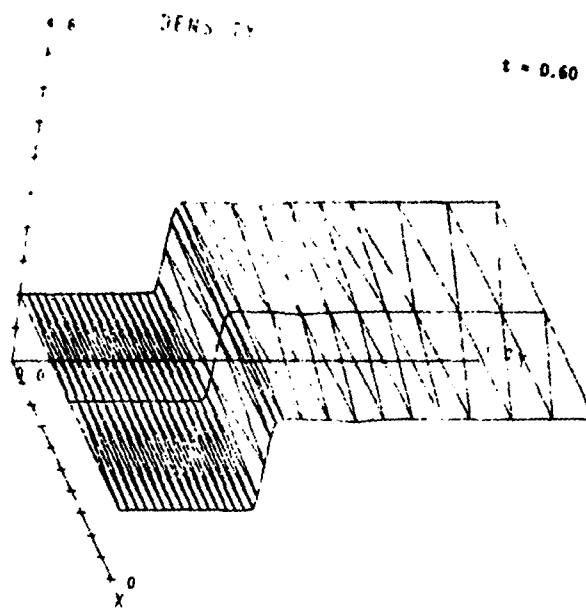


Figure 57.

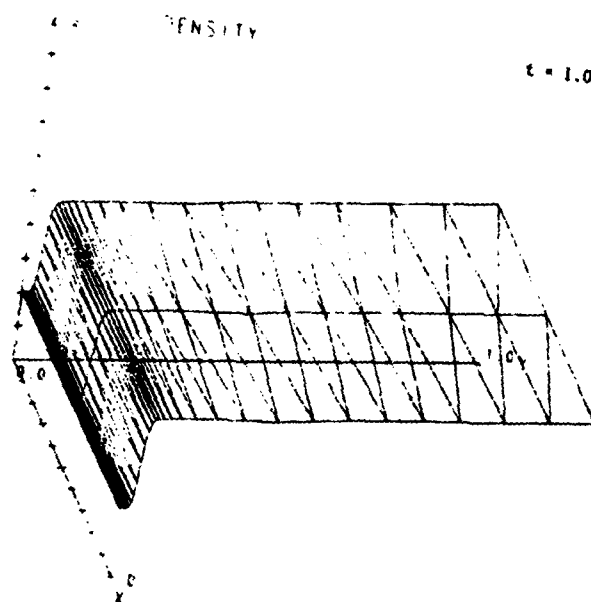


Figure 58.

MFE Solutions of Laminar Navier-Stokes Equations for an Experimental Plane Shock of Deschambault and Glass Reflecting Against a Vertical Wall. ($M_s = 2.05$, $\theta = 90^\circ$, $p_+ = 150$ torr, $\rho_+ = 3.23 \times 10^{-4} \text{g/cm}^3$ in Argon.) A 3×31 MFE Grid is Used.

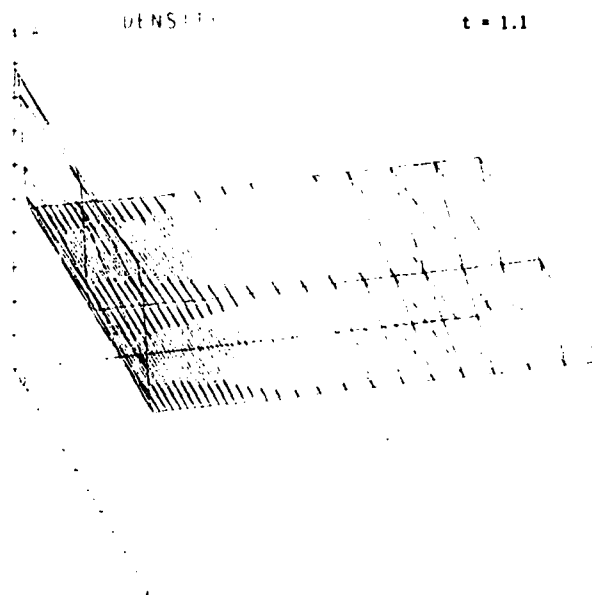


Figure 59.

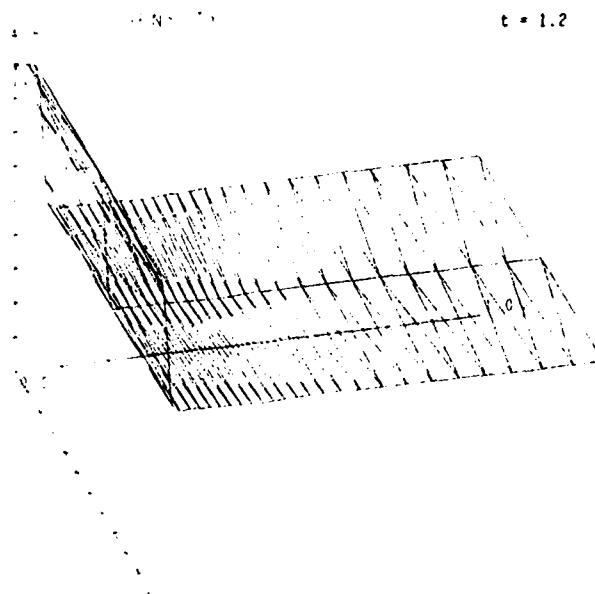


Figure 60.

MFE Solutions of Laminar Navier-Stokes Equations for An Experimental Plane Shock of Deschambault and Glass Reflecting Against a Vertical Wall. ($M_s = 2.05$, $\theta = 90^\circ$, $p_+ = 150$ torr, $\rho_+ = 3.23 \times 10^{-4} \text{ g/cm}^3$ in Argon.) A 3×31 MFE Grid is Used.

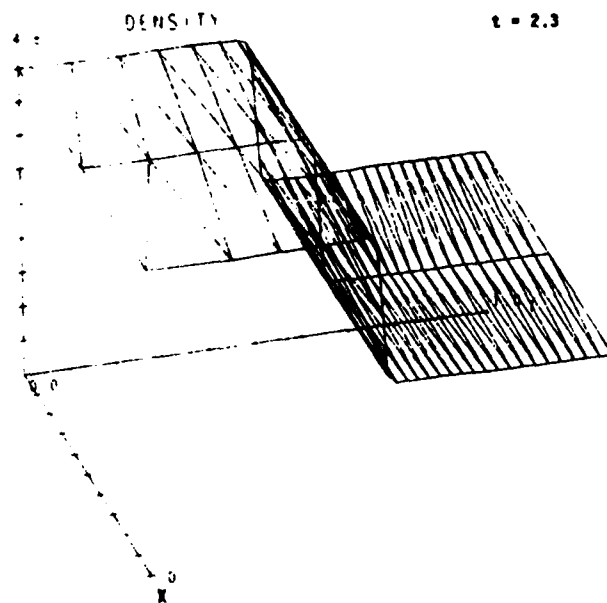


Figure 61. MFE Solutions of Laminar Navier-Stokes Equations for An Experimental Plane Shock of Deschambault and Glass Reflecting Against a Vertical Wall. ($M_s = 2.05$, $\theta = 90^\circ$, $p_+ = 150$ torr, $\rho_+ = 3.23 \times 10^{-4} \text{ g/cm}^3$ in Argon.) A 3×31 MFE Grid is Used.

t = 2.3

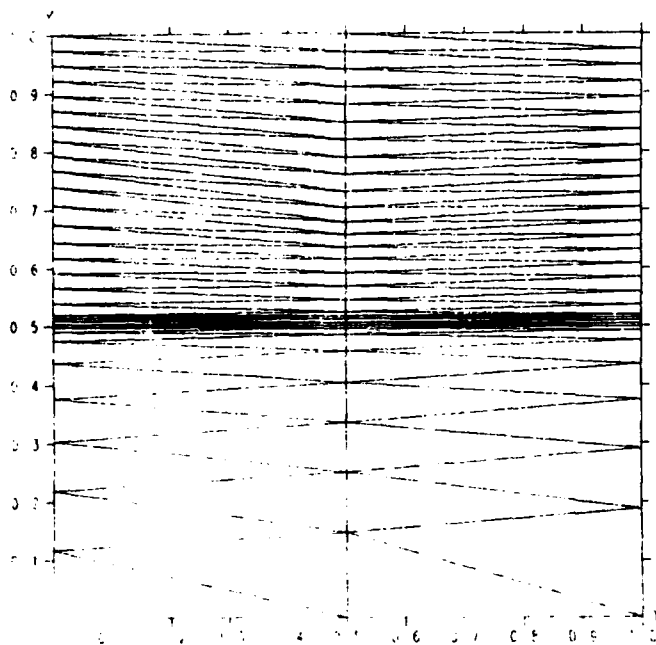


Figure 62. Project of MFE Grid Mesh on the x-y Plane for an Experimental Plane Shock of Deschambault and Glass Reflecting Against a Vertical Wall. ($M_s = 2.05$, $\theta = 90^\circ$, $p_+ = 150$ torr, $\rho_+ = 3.23 \times 10^{-4} \text{ g/cm}^3$ in Argon.) A 3×31 MFE Grid is Used.

at $t = 0.35$ have a regular profile. At $t = 0.44$ the formation and subsequent shedding of eddies are becoming apparent. These are formed and evolved according to the physically inadequate laminar dissipation processes in the present Navier-Stokes solutions and not by numerical dissipation. Analysis of vorticity generation rates indicates clearly that a turbulent model of the physical dissipation in the boundary layer is required in order to model this system according to physical reality. We nevertheless seem to be computing the early onset of turbulent behavior.

Mostly, this example shows an apparent capacity of the MFE method to attempt to resolve extremely micro-scale dissipation processes simultaneously with the macroscopic flow features. In this sample problem, it was undoubtedly the physics model which requires improvement more than the numerics. Because local turbulent dissipation rates exceed laminar rates by large factors, it is likely that this experimental test example imposes more severe demands upon the PDE method than will be encountered in more realistic physical models of real shock environments (which have much larger-than-laminar dissipation rates).

In order to verify that the complex behavior in this example was truly associated with vorticity generation in the boundary layer, this same incident shock was propagated into, and reflected from, a vertical wall. Fluid shears do not occur in this example, and the MFE solutions appear in Figures 56 to 62. The shock profiles remain perfectly planar (to many significant figures) because only compressive and expansive forces act in this reflection process. Neither numerical dissipation nor anomalous vorticity effects were perceptible in these MFE solutions. It was also validated that the Rankine-Hugoniot and Taylor solutions of the steady reflected shock profiles were obtained in these MFE solutions.

SUMMARY

The report above describes all significant results of this three-year investigation of the basic MFE method and its properties. Both the promise and the problems which may require extensive additional research have been indicated.

REFERENCES

1. Miller, K. and R. Miller, "Moving Finite Elements, Part I and II," SIAM J. of Num. Anal., 1019-57, Vol. 18, No. 6, December 1981.
2. Gelinas, R.J., S.K. Doss and K. Miller, "The Moving Finite Element Method: Applications to General Partial Differential Equations with Multiple Large Gradients," J. Comp. Phys., 40, No. 1, pg. 202, March 1981.
3. Gelinas, R.J., S.K. Doss, J.P. Vajk, J. Djomehri and K. Miller, "Moving Finite Elements in 2-D," Proceedings, Vol. 1, pg. 58-60, edited by R. Vichnevetsky, 10th IMACS World Congress on Systems Simulation and Scientific Computation, Montreal, Canada, August 8-13, 1982.
4. Gelinas, R.J., "Moving Finite Elements in 2-D," First Annual Progress Report for AFOSR contract F49620-81-C-0073, June 7, 1982.
5. Wathen, A.J., "Moving Finite Elements and Oil Reservoir Modeling," Ph.D. Dissertation, University of Reading, Reading, England, May 1984.
6. Djomehri, J. and K. Miller, "A Moving Finite Element Code for General Systems of PDE's in 2-D," Technical Report PAM-57, Center for Pure and Applied Mathematics, University of California, Berkeley, California, October 12, 1981.
7. Gelinas, R.J. and S.K. Doss, "The Moving Finite Element Method: A Semi-Automatic Solver for Diverse PDE Applications," Advances in Computer Methods for Partial Differential Equations--IV, pg. 230-239, edited by R. Vichnevetsky and R.S. Stepleman, Proceedings, Fourth IMACS International Symposium on Computer Methods for Partial Differential Equations, Lehigh University, Bethlehem, Pennsylvania, June 30-July 2, 1981.
8. Gelinas, R.J. and S.K. Doss, "The Moving Finite Element Method: 1-D Transient Flow Applications," Proceedings, Vol. 1, pg. 156-158, edited by R. Vichnevetsky, 10th IMACS World Congress on Systems Simulation and Scientific Computation, Montreal, Canada, August 8-13, 1982.
9. Gelinas, R.J., S.K. Doss and N.N. Carlson, "Moving Finite Element Research for Shock Hydrodynamics, Continuum Mechanics and Combustion," Proceedings, First Army Conference on Applied Mathematics and Computing, George Washington University, Washington, DC, May 8-11, 1983.
10. Deschambault, R.L. and I.I. Glass, "An Update on Nonstationary Oblique Shock Wave Reflections: Actual Isopycnics and Numerical Experiments," Preprint, Institute for Aerospace Studies, University of Toronto, Toronto, Ontario, Canada, 1983.

ADDITIONAL INFORMATION

JOURNAL PUBLICATIONS

1. Gelinas, R.J., S.K. Doss, and N.N. Carlson, "Moving Finite Element Research for Shock Hydrodynamics, Continuum Mechanics and Combustion," Proceedings of First Army Conference on Applied Mathematics and Computing, George Washington University, Washington, DC, May 8-11, 1983.
2. Gelinas, R.J. and S.K. Doss, "The Moving Finite Element Method: One-Dimensional Transient Flow Applications," Proceedings, 10th IMACS World Congress on Systems Simulation and Scientific Computation, Montreal, Canada, August 8-13, 1982.
3. Gelinas, R.J., S.K. Doss, J.P. Vajk, J. Djomehri, and K. Miller, "Moving Finite Elements in 2-D," Proceedings, 10th IMACS World Congress on Systems Simulation and Scientific Computation, Montreal, Canada, August 8-13, 1982.
4. Gelinas, R.J., S.K. Doss, J.P. Vajk, J. Djomehri, and K. Miller, "The Moving Finite Element Method: Fluid Dynamics Examples," Proceedings, 10th IMACS Congress, Montreal, Canada, August 8-13, 1982.
5. Gelinas, R.J. and S.K. Doss, "The Moving Finite Element Method: Strong Shock and Penetration Applications," Lecture Notes in Engineering - 3, pg. 192-209, edited by C.A. Brebbia and S.A. Urszag, Proceedings, Army Research Office Workshop on Computational Aspects of Penetration Mechanics, Ballistics Research Laboratory, Aberdeen, MD, April 27-29, 1982.
6. Gelinas, R.J., "Moving Finite Element Method in 2-D," Proceedings, 1982 Army Numerical Analysis and Computers Conference, Vicksburg, MS, February 3-4, 1982.
7. Gelinas, R.J. and S.K. Doss, "The Moving Finite Element Method: A Semi-Automatic Solver for Diverse PDE Applications," Advances in Computer Methods for Partial Differential Equations - IV, pg. 230-239, edited by R. Vichnevetsky and R.S. Stepleman, Proceedings, Fourth IMACS International Symposium on Computer Methods for Partial Differential Equations, Lehigh University, Bethlehem, PA, June 30-July 2, 1981.
8. Prosnitz, D., R.A. Haas, S.K. Doss, and R.J. Gelinas, "Two-Dimensional Numerical Model Of a Free Electron Laser Amplifier," to appear in the J. of Quantum Electronics. (Summary presented at the Conference on Lasers and Electro-Optics (CLEO-81), Washington, DC, June 10-12, 1981.)
9. Gelinas, R.J., S.K. Doss, and K. Miller, "The Moving Finite Element Method: Applications to General Partial Differential Equations with Multiple Large Gradients," J. Comp. Phys., 40, No. 1, pg. 202, March 1981.

PROFESSIONAL PERSONNEL ASSOCIATED WITH THE RESEARCH EFFORT

Mr. Neil N. Carlson (Mr. Carlson has a B.S. degree in Mathematics, and is presently enrolled as a graduate student in Mathematics at U.C. Berkeley.)

Dr. M. Jahed Djomehri (Dr. Djomehri is a student of Professor Keith Miller of U.C. Berkeley, and has a Ph.D. in Nuclear Engineering and in Mathematics.)

Dr. Said K. Doss (Ph.D., Applied Mathematics)

Dr. Robert J. Gelinas (Ph.D., Nuclear Engineering)

Dr. J. Peter Vajk (Ph.D., Physics)

Programmers (J. Griffith, M. Medin, D. Rapoport, D. Robles, U. Ofiesh, and S. Schell)

INTERACTIONS (COUPLING ACTIVITIES)

Papers presented at meetings and conferences

- 1984: Kinetic Energy - Target Interaction Workshop, "Moving Finite Elements - An Overview for Shock/Impact Physics Applications."
- 1983: Exxon Research Workshop, "Mathematical Modeling of Physical Phenomena Using Moving Finite Elements."
- DNA Airblast Review Meeting, "Moving Finite Element Methods."
- Los Alamos National Laboratory Workshop, "Fluid Interface Instabilities and Front Tracking."
- First Army Conference on Applied Mathematics and Computing, "Moving Finite Element Research."
- 1982: Army Numerical Analysis and Computers Conference, "Moving Finite Elements in 2-D."
- Army Research Office Workshop on Computational Aspects of Penetration Mechanics, "The Moving Finite Element Method: Strong Shock and Penetration Mechanics Applications."
- 10th IMACS Congress, "Moving Finite Elements in 2-D."
- 10th IMACS Congress, "The Moving Finite Element Method: One-Dimensional Transient Flow Applications."
- 1981: Fourth IMACS International Symposium on Computer Methods for Partial Differential Equations, "The Moving Finite Element Method: A Semi-Automatic Solver for Diverse PDE Applications."

1981: LASL Adaptive Mesh Workshop, "The Moving Finite Element Method: Implementation of a 2-D Code."

SIAM Meeting, "Solution of the Gas Dynamics Equations in 1-D by the Moving Finite Element Method."

Consultive functions to other agencies

1. Eglin Air Force Base; former contract to investigate the application of the MFE method in 2-D to armor penetration effects; contact: Major Guy Spitale.
2. Defense Nuclear Agency; under contract to investigate the application of the MFE method in 2-D to airblast effects; contact: Dr. George Ullrich.
3. EG&G-Idaho; former contract for User Instruction Manual on the DYLA - A Moving Finite Element Code in 1-D; contact: Mr. Robert Pence.

END

FILMED

10-84

DTIC